Cell Reports
Methods

Article

De-erosion of X chromosome dosage compensation by the editing of *XIST* regulatory regions restores the differentiation potential in hPSCs

Graphical abstract

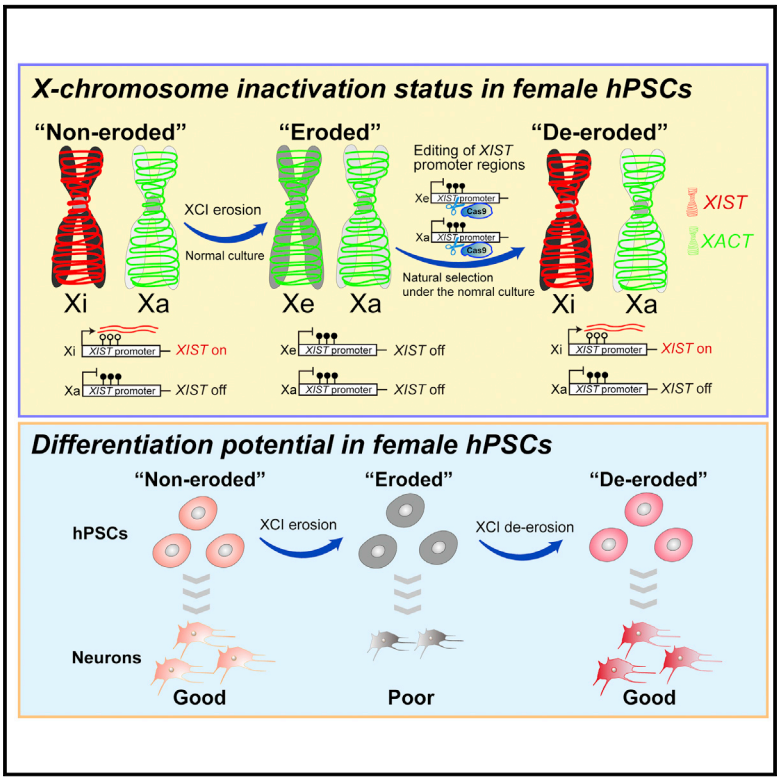

Highlights

- Erosion of XCI by *XIST* silencing affects neuronal differentiation in female hPSCs
- Editing of *XIST* promoter regions by Cas9 nuclease causes DNA demethylation
- Editing of *XIST* promoter regions induces *XIST* reactivation and de-erosion of XCI
- De-erosion of XCI restores differentiation potential in female hPSCs

Authors

Nami Motosugi, Akiko Sugiyama, Chisa Okada, ..., Hidenori Akutsu, Shinji Hadano, Atsushi Fukuda

Correspondence

fa972942@tsc.u-tokai.ac.jp

In brief

Erosion of X chromosome inactivation (XCI) by *XIST* silencing is irreversible in female hPSCs. Motosugi et al. demonstrate that editing of *XIST* promoter regions with hyper DNA methylation by Cas9 nuclease causes demethylation and *XIST* reactivation. *XIST* reactivation results in the de-erosion of XCI and restoration of differentiation potential.

Motosugi et al., 2022, Cell Reports Methods *2*, 100352
December 19, 2022
https://doi.org/10.1016/j.crmeth.2022.100352

CellPress

Cell Reports Methods

CellPress
OPEN ACCESS

Article

De-erosion of X chromosome dosage compensation by the editing of *XIST* regulatory regions restores the differentiation potential in hPSCs

Nami Motosugi,[1,6] Akiko Sugiyama,[1,6] Chisa Okada,[4] Asako Otomo,[1,2,3] Akihiro Umezawa,[5] Hidenori Akutsu,[5] Shinji Hadano,[1,2,3] and Atsushi Fukuda[1,2,3,5,7,*]

[1]Department of Molecular Life Sciences, Division of Basic Medical Science and Molecular Medicine, Tokai University School of Medicine, Isehara, Kanagawa, Japan
[2]The Institute of Medical Sciences, Tokai University, Isehara, Kanagawa, Japan
[3]Micro/Nano Technology Center, Tokai University, Hiratsuka, Kanagawa, Japan
[4]Support Center for Medical Research and Education, Tokai University School of Medicine, Isehara, Kanagawa, Japan
[5]Center for Regenerative Medicine, National Center for Child Health and Development, Tokyo, Japan
[6]These authors contributed equally
[7]Lead contact
*Correspondence: fa972942@tsc.u-tokai.ac.jp
https://doi.org/10.1016/j.crmeth.2022.100352

MOTIVATION Erosion of X chromosome inactivation (XCI) is caused by *XIST* silencing. Erosion of XCI is inevitable and irreversible in female hPSCs, causing the limitation of female hPSC utilities. However, there are no reliable and reproducible methods to reactivate *XIST*, leading to de-erosion in female hPSCs. To resolve the long-standing problem in female hPSCs, we developed methods to restore *XIST* expression in a monoallelic manner, resulting in the de-erosion of XCI. De-erosion of XCI is beneficial to various applications of female hPSCs including patient-specific iPSCs.

SUMMARY

Human pluripotent stem cells (hPSCs) regularly and irreversibly show the erosion of X chromosome inactivation (XCI) by long non-coding RNA (lncRNA) *XIST* silencing, causing challenges in various applications of female hPSCs. Here, we report reliable methods to reactivate *XIST* with monoallelic expression in female hPSCs. Surprisingly, we find that the editing of *XIST* regulatory regions by Cas9-mediated non-homologous end joining is sufficient for the reactivation of *XIST* by endogenous systems. Proliferated hPSCs with *XIST* reactivation show XCI from an eroded X chromosome, suggesting that hPSCs with normal dosage compensation might lead to a growth advantage. Furthermore, the use of targeting vectors, including the *XIST* regulatory region sequences and selection cassette, enables *XIST* reactivation in hPSCs with high efficiency. *XIST*-reactivated hPSCs can show the restoration of differentiation potential. Thus, our findings demonstrate that *XIST* re-expression is a beneficial method to maximize the use of female hPSCs in various applications, such as proper disease modeling.

INTRODUCTION

The generation of human pluripotent stem cells (hPSCs), including embryonic stem cells (ESCs) and induced pluripotent stem cells (iPSCs), has proved to be important for numerous medical applications and drug discoveries and elucidated basic human biology *in vitro* (Takahashi et al., 2007; Thomson et al., 1998; Yamanaka, 2020). Although hPSCs are a powerful tool to understand biological phenomena based on genetic background, "erosion" of X chromosome dosage compensation in female hPSCs is an inevitable problem, induced by the irreversible silencing of the long non-coding RNA (lncRNA) *XIST*; GenBank: NG_016172. *XIST* is expressed from one of two X chromosomes to archive X chromosome inactivation (XCI), and the expression is maintained in female somatic cells (Augui et al., 2011; Penny et al., 1996). Previous studies have shown that *XIST* repression in female hPSCs causes the overexpression of X-linked genes and results in a poor differentiation ability (Anguera et al., 2012; Fukuda et al., 2021; Mekhoubad et al., 2012; Patel et al., 2017). Therefore, *XIST* dysregulation may be one of the largest and most underestimated sources of variability hampering reproducibility and disease modeling in female hPSC research.

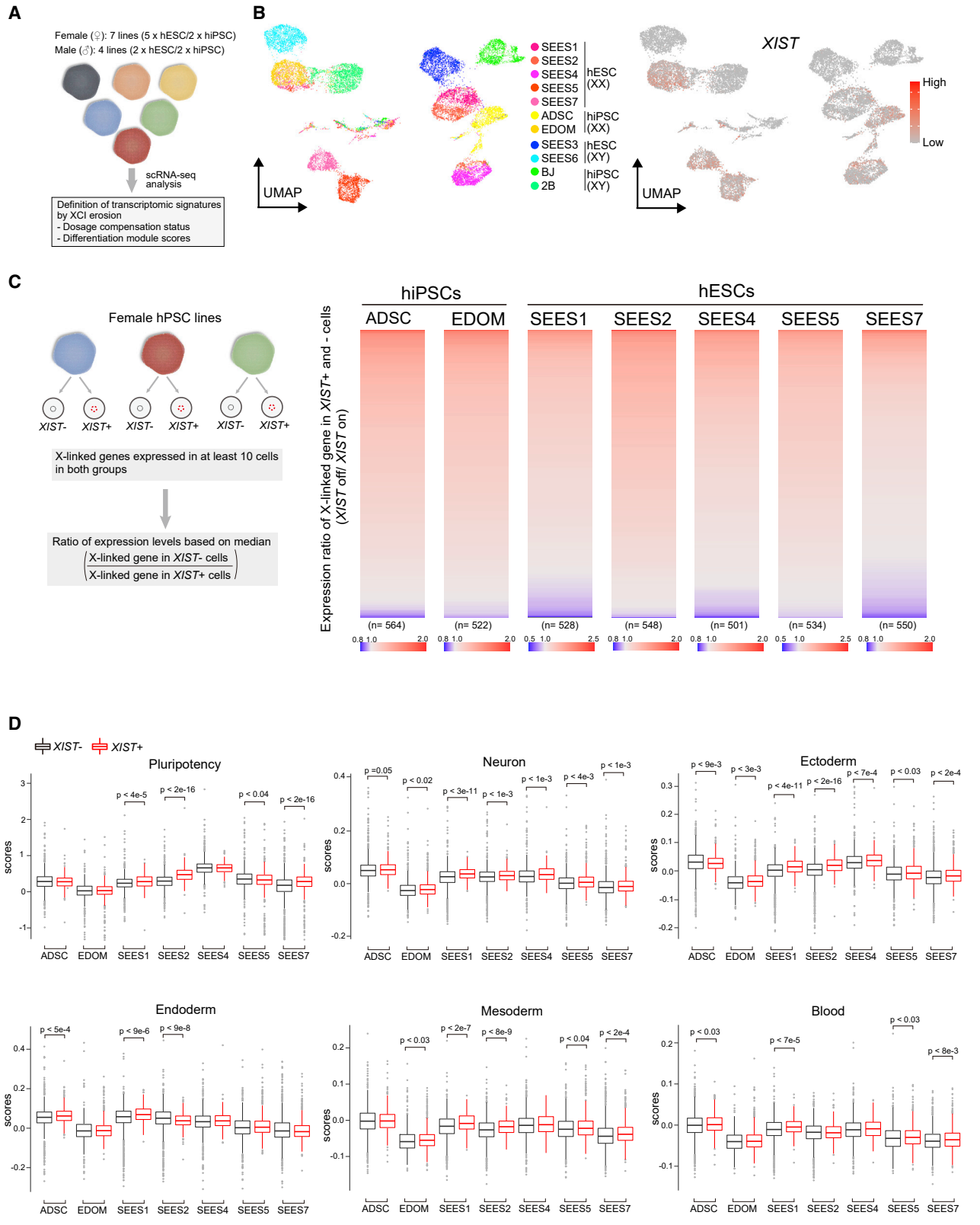

(legend on next page)

While naive conversion from hPSCs has been shown to reactivate *XIST*, the efficiency depends on the genetic background (Guo et al., 2017; Sahakyan et al., 2017). Furthermore, the selection of the *XIST* reactivation allele is inconsistent when naive cells revert to the primed hPSC state (An et al., 2020; Sahakyan et al., 2017). Thus, unless effective solutions are identified, *XIST* silencing can limit the deployment of female hPSC lines in translational efforts. If women are to equally benefit from the potential revolution in human cell therapies, and if hPSCs are to be used to their full potential, it is essential to develop a new method to restore XCI in the eroded X chromosome.

In the present study, we highlighted the importance of *XIST* expression in female hPSCs upon differentiation. To reduce the undesirable effects of irreversible *XIST* repression, we have developed a novel and reproducible method to restore XCI by editing *XIST* regulatory elements in female hPSCs, leading to *XIST* reactivation by the endogenous expression system. Female hPSCs with *XIST* reactivation, including X-linked disease iPSCs, undergo restoration of differentiation ability. Thus, the method of reactivating *XIST* expression is useful for evaluating appropriate phenotypes, including in disease modeling applications, in female hPSCs.

RESULTS

XIST repression in female hPSCs commonly affects the differentiation modules but not the core pluripotency factors

To obtain insights into transcriptomic features based on the XCI status without considering the effect of the genetic background, we performed single-cell RNA sequencing (scRNA-seq) analysis using 11 hPSC lines (seven females and four males), including both ESCs and iPSCs. In female hPSC lines, to compare the transcriptional effects driven by XCI erosion, we used a mixed population composed of *XIST*+ and *XIST*– cells with the same passage number (Figure 1A). Dimensionality reduction analysis (Stuart et al., 2019) by uniform manifold approximation and projection (UMAP) revealed that the genetic background was a strong driver for cluster segregation (Figure 1B). The *XIST* expression status and derivational origins were not major drivers of cluster segregation (Figure 1B). Since UMAP analysis was performed using all transcripts, to examine the effect of *XIST* expression on the expression dosage of X-linked genes, we calculated the median expression levels in individual X-linked genes between *XIST*+ and *XIST*– cells in each female hPSC line. The comparison analysis of the median expression levels showed the tendency of over-dosage of X-linked genes in *XIST*– cells in all lines examined (Figure 1C). Moreover, the average expression levels of X-linked genes in *XIST*– hPSCs were significantly upregulated compared with those in *XIST*+ and male hPSCs (Figure S1A), consistent with the findings from previous reports (Anguera et al., 2012; Mekhoubad et al., 2012).

Next, we investigated if the *XIST* expression status impacts the expression of the core pluripotency factors OCT4, SOX2, and NANOG (Wang et al., 2012) in hPSCs. Although the extent of expression of each gene differed among the lines, especially that of NANOG, we did not observe statistically significant differences between the factors in *XIST*+ and *XIST*– cells (Figure S1B). However, we found that the expression levels of UTF1, linked to the heterogeneity of the hPSC population (Tan et al., 2007), greatly differed among the lines (Figure S1C). The expression levels in *XIST*+ cells were significantly higher than those in *XIST*– cells in the SEES2 line (Figure S1C). Interestingly, UMAP analysis in SEES2 showed an *XIST*+ cluster with UTF1 expression (Figure S1D), suggesting that extensive erosion might be associated with the dysregulation of pluripotency-related gene expression.

Findings from previous studies have suggested that hPSC lines with strong XCI erosion, as evaluated using the DNA methylation status, showed poor differentiation scores, which were calculated using the expression levels in a subset of genes (module) (Patel et al., 2017; Saelens et al., 2018). However, given that the genetic background substantially affects the transcriptomic features, including the erosion status, in hPSCs (Figure 1C), the score comparisons between *XIST*+ and *XIST*– cells in the same line would indicate the direct effect of *XIST* suppression. We calculated the differentiation scores based on findings from previously validated gene sets in hPSCs (Bock et al., 2011) as well as the core pluripotency factors (OCT4/SOX2/NANOG). Interestingly, different from the results in individual gene-expression statuses (Figure S1B), the core pluripotency module showed significant differences between *XIST*+ and *XIST*– cells in some lines, but the tendency depended on the lines (Figure 1E). In differentiation modules, the endoderm scores also showed inconsistent tendencies in each line (Figure 1E). However, in other lineages, the differentiation scores of *XIST*+ cells tended to be higher than those of *XIST*– cells in most lines (Figure 1E). Especially, the neuronal scores of *XIST*+ cells were higher than those of *XIST*– cells in all lines, and the differences in six out of seven lines were statistically significant (Figure 1E). These results indicate that *XIST* repression does not lead to a consistent tendency in the core pluripotency factors, but it commonly affects the differentiation modules, with a particularly negative effect on neuronal differentiation.

The *XIST* expression status is linked to the stages of neuronal differentiation

Next, to address whether the molecular characteristics of the neuronal lineages of hPSCs are linked to the phenotypes, we

Figure 1. *XIST* repression commonly affects the differentiation modules, but not core pluripotency, in female hPSCs

(A) Analysis scheme of single-cell RNA sequencing (scRNA-seq) analysis in 11 hPSC lines.

(B) UMAP analysis of 11 hPSC lines. Left: UMAP based on genetic background. Right: *XIST* expression status. The heatmap shows the expression levels.

(C) Expression ratio of X-linked genes in *XIST*+ and *XIST*– female hPSCs based on median levels. The X-linked genes expressed in at least ten cells in both *XIST*+ and *XIST*– groups were used for the analysis. The heatmap shows the ratio (*XIST*–/*XIST*+), indicating that red color is overexpressed in *XIST*– cells. n indicates the number of X-linked genes analyzed.

(D) Module scores related to differentiation and pluripotency. The pluripotency module was based on the expression of OCT4, SOX2, and NANOG (Wang et al., 2012). The differentiation markers previously identified were used for the module calculation (Bock et al., 2011). The comparisons of each module were based on the *XIST* expressions status. p values were calculated using Wilcoxon's rank-sum test.

conducted spinal motor neuron differentiation using defined protocols of two-dimensional culture (Klim et al., 2019). We first evaluated the XCI status in differentiating neurons by immunofluorescence with H3K27me3/H2AK119ub, XCI hallmarks that overlap with the *XIST* RNA (Anguera et al., 2012; Fukuda et al., 2021; Motosugi et al., 2021; Sahakyan et al., 2017), and neuronal cell markers. Unexpectedly, immunofluorescence combined with *XIST* RNA-fluorescence *in situ* hybridization (immuno-FISH) analysis revealed that a complete overlap of *XIST* RNA with XCI hallmarks (H3K27me3/H2AK119ub) was observed only in hPSCs, not in differentiating and primary cells (Figures S1E and S1F). In particular, most motor neurons (MNs) lacked H2AK119ub modification (Figures S1E and S1F). These results indicated that epigenetic modification on Xi depends on cell types even when *XIST* is statedly expressed. Thus, we conducted an immuno-FISH assay to evaluate if the *XIST* expression status is linked to the neuronal differentiation stage.

Seven female hPSC lines, composed of a mixture of *XIST*+ and *XIST*– cells in each line, were differentiated, and the status was analyzed at two time points (neuronal progenitor/post-mitotic phases) (Figure S2A). To exclude the possibility that the starting number of *XIST*+ or *XIST*– cells affects the differentiation status evaluation, we counted the number of marker+/*XIST*+ to *XIST*+ cells or marker+/*XIST*– to *XIST*– cells in differentiated cells. On day 6 of differentiation, the population of cells with *PAX6*+/*XIST*+ was significantly smaller than that with *PAX6*+/*XIST*–in most lines (Figures S2B and S2C). However, on day 10 of differentiation, among the seven female hPSC lines, five showed a significantly higher proportion of *ISL1*+/*XIST*+ cells than of *ISL1*+/*XIST*– cells (Figures S2B and S2C), indicating that *XIST* repression negatively affected the generation of post-mitotic MNs.

Next, we examined if differentiation into post-mitotic neuronal cells in cortical organoid development is also linked to the *XIST* expression status (Figure S2D). Immuno-FISH analysis showed that considerably varied phenotypes and organoids from some lines formed a typical morphology, but no marker was detected in male or female lines (Figures S2E–S2G). In the female hPSC lines, at day 90 of differentiation from hPSCs, three lines (ADSC-iPS, SEES1, and SEES7) expressed all markers (SATB2/TBR1/CTIP2) (Bhaduri et al., 2020; Thomsen et al., 2016; Velasco et al., 2019) in at least three organoids (Figures S2F and S2G). Consistent with the results observed in MNs, immuno-FISH analysis in the three female lines revealed that the differentiation potential of *XIST*+ cells toward cortical neuron markers (SATB2 and TBR1) tended to be greater than that of *XIST*– cells (Figure S2G).

To evaluate the differentiation status of cortical organoids based on *XIST* expression in a less biased manner, we analyzed the scRNA-seq data using the HUES66 female line (Velasco et al., 2019). We first examined whether differentiated cells also exhibit the over-dosage of X-linked genes in *XIST*– cells. Since the differentiating cells show a wide transcriptome diversity (Thomsen et al., 2016), we focused on the cells in the same cluster identified by markers (Bhaduri et al., 2020; Thomsen et al., 2016). We examined the median expression levels of individual X-linked genes in *XIST*+ and *XIST*– groups in classified cell types (Figures S2H and S2I). The analysis revealed that the over-dosage of X-linked genes in various cell types derived from HUES66, especially in the radial glial cell population, showed a strong tendency for over-dosage (Figure S2J). These results indicated that *XIST* repression leads to the overexpression of X-linked genes in differentiating cells, consistent with the findings from previous reports (Patel et al., 2017). Next, we calculated the percentage of *XIST*+ and *XIST*– cells in each cell type and compared the ratio. Interestingly, the cells from the initial phase of neuronal differentiation, such as radial glial cells, tended to include a large population in *XIST*– cells compared with that of *XIST*+ cells (Figure S2K), whereas the population of *XIST*+ cells was larger among neuronal cells (Figure S2K), and the *XIST* gene was identified as a cluster marker of CTIP2 excitatory neurons (Table S1). In the neurons, the number of cells marked by CCNI or NEUROD2 was greater in the *XIST*– population (Figure S2K). However, trajectory analysis showed that these populations showed a low pseudotime, indicating the initial differentiation phases (Figure S2L). Consistent with the results observed in MNs (Figure S2C), in cortical differentiation from hPSCs, the status of *XIST*+ cells tended to be more matured compared with that of *XIST*– cells. Taken together, considering findings from previous reports that showed that *XIST* repression is irreversible before/after differentiation and negatively affects the differentiation potential of female hPSCs (Anguera et al., 2012; Fukuda et al., 2021; Mekhoubad et al., 2012; Salomonis et al., 2016; Vallot et al., 2015), our findings demonstrated that the high module scores of neuronal lineage in *XIST*+ female hPSCs are linked to a phenotype.

Experimental results using female hPSCs with autosomal gene mutations differ based on the *XIST* expression status in hPSCs

The deficiency of the *de novo* DNA methyltransferases DNMT3A and 3B impairs MN differentiation in male hPSCs (Ziller et al., 2018). Recently, we found that the deletion of both enzymes prevents *XIST* silencing in female hPSCs (Fukuda et al., 2021). The findings from these studies led us to question whether the *XIST* expression status in female hPSCs with autosomal gene defects affects the experimental results. To address this, we generated a DNMT3A/3B double-mutant knockout (dKO) using *XIST*+ or *XIST*– EES5 lines (Figures 2A and 2B).

We first checked the transcriptome status by bulk RNA-sequencing in each dKO line. Hierarchical clustering analysis using all transcripts, including autosomal genes, showed that the dKO samples were close to each other, regardless of the *XIST* expression status (Figure 2C). However, when clustering analysis was conducted using X-linked genes, the clusters were formed based on the *XIST* expression status (Figure 2C), indicating that the expression status of X-linked genes depends on the *XIST* expression status rather than the loss of *de novo* DNA methyltransferases in the SEES5 line.

The MN differentiation experiments using immuno-FISH revealed that *XIST* was not reactivated in the majority of MNs upon DNMT3A/3B deletion (Figures 2D and 2E). Meanwhile, MNs derived from *XIST*+ cells retained *XIST* expression (Figures 2D and 2E). Surprisingly, on day 14, the number of ISL1+ cells was >60% in both *XIST*+ lines (Figures 2D and 2F),

CellPress
OPEN ACCESS

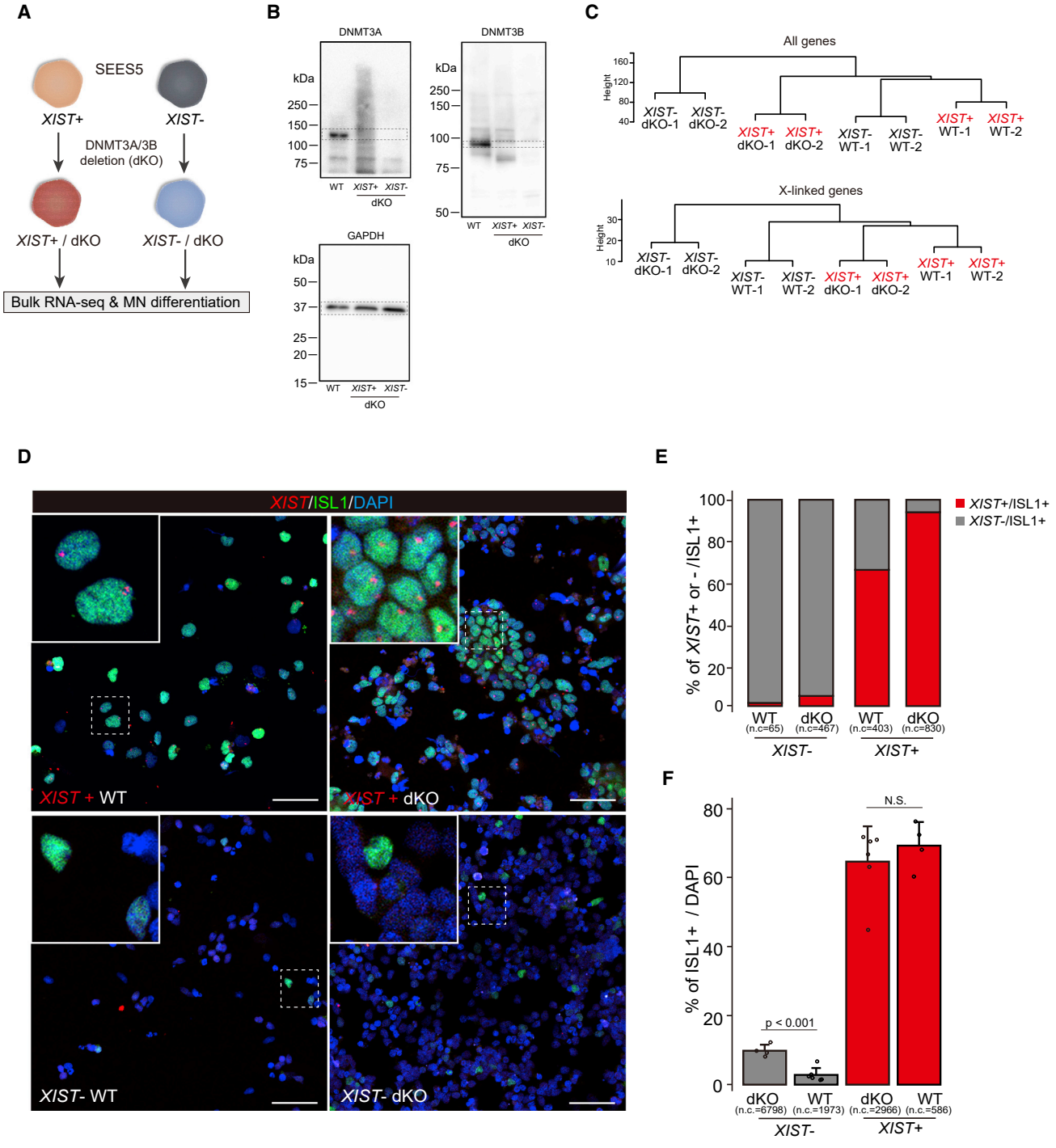

Figure 2. The X chromosome inactivation (XCI) status affects the results of the autosomal gene functional assay of female hPSCs

(A) Experimental scheme for the generation of a DNMT3A/3B double-mutant knockout (dKO) line. The *XIST*+ or *XIST*– SEES5 line was used to examine if the XCI status affects MN differentiation.

(B) Western blot analysis, with GAPDH used as the loading control.

(C) Bulk RNA-seq analysis. Hierarchical clustering analysis using all genes (top) and X-linked genes (bottom).

(D) Immuno-FISH analysis of MNs. *ISL1* immunofluorescence combined with *XIST* RNA-FISH (immuno-FISH) analysis was performed to evaluate the differentiation efficiency. Representative images of the *ISL1*- and *XIST* expression statuses in the dKO and wild-type (WT) lines, respectively. Scale bar represents 50 μm.

(E and F) Quantification results of the immuno-FISH analysis. The percentages of *XIST*+ or *XIST*– cells with ISL+ are shown (E). The differentiation efficiencies evaluated using ISL1+ cells are shown (F). Each dot and n.c. indicate the percentage in the observed area and the total number of cells analyzed, respectively. Error bars show standard deviations. p values were calculated using Student's t test.

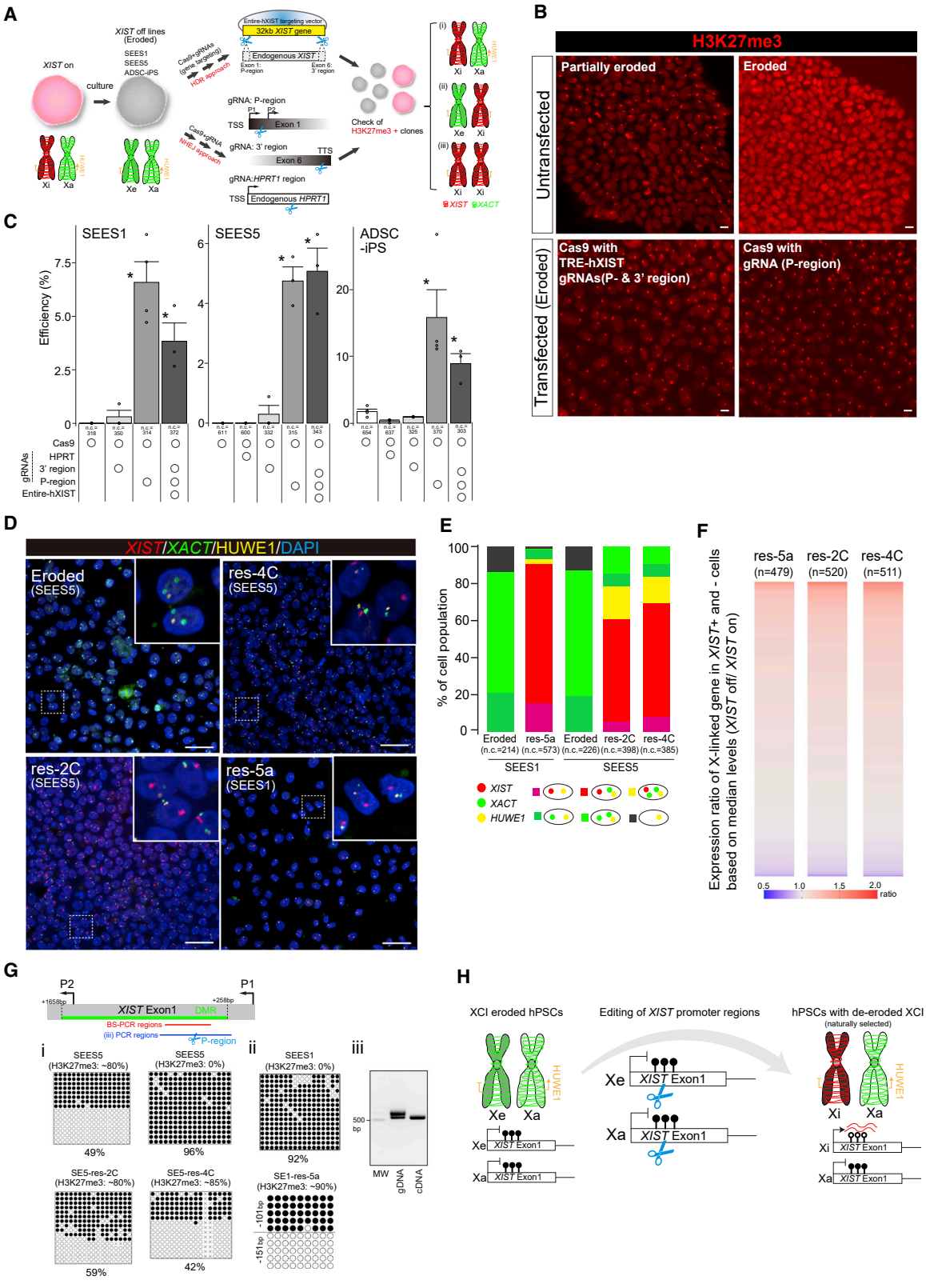

(legend on next page)

and the efficiency of the dKO line was comparable to that of wild type (Figures 2D and 2F). However, the efficiency markedly reduced in *XIST*– lines (<10% in both lines; Figures 2D and 2F). Furthermore, the dKO line in *XIST*– cells exhibited a significantly higher efficiency compared with the wild-type *XIST*– line (Figures 2D and 2F). However, given that *XIST* repression causes XCI erosion, we cannot conclude whether the findings using *XIST*– lines result from DNMT3A/3B dysfunction and/or XCI erosion. Taken together, these results demonstrated that the XCI status in female hPSCs affects not only X chromosome dosage compensation but also the outcomes of the autosomal gene functional assay.

Editing of *XIST* regulatory elements leads to the de-erosion of female hPSCs

Thus far, our findings have revealed the importance of *XIST* expression in the cellular phenotype of female hPSCs. However, there is no reliable method to restore *XIST* expression in the current culture system of hPSCs. Even when naive conversion is applied, the efficiency depends on the genetic background (Guo et al., 2017; Sahakyan et al., 2017). Recently, we found that the endogenous reactivation of *XIST* by the clustered regularly interspaced short palindromic repeats (CRISPR) activation system can induce *XIST* transcripts, but the *XIST* RNA does not act in *cis* (Fukuda et al., 2021; Motosugi et al., 2021), suggesting that epigenetic modifications affecting *XIST* transcript behavior might be altered in the *XIST* gene of eroded female hPSCs. To overcome these challenges, we developed two new approaches to reacquire the *XIST* function via an endogenous transcription system. The first approach is based on a gene-targeting strategy using CRISPR-Cas9-mediated homology-directed repair (HDR) (Doudna and Charpentier, 2014), for which we introduced a new *XIST* gene into the original region (Figure 3A). In the second approach, we tested the possibility of non-homologous end joining (NHEJ) (Doudna and Charpentier, 2014)-mediated gene reactivation (Figure 3A). Since the findings of a recent study suggested that Cas9-mediated double-strand breaks (DSBs) induce *de novo* DNA methylation (DNAme) around guide RNA (gRNA)-targeting sites (Cali et al., 2019), and this indicates that epigenetic status alters before/after DSBs, we inferred that if an opposite event, DNA de-methylation, occurs in *XIST*– female hPSCs during NHEJ, *XIST* repressed by DNAme would be reactivated. For the HDR approach, we generated a targeting vector containing the entire 32 kb human *XIST* gene (Entire-hXIST; Figure 3A). In the NHEJ approach, we designed three sgRNA regions; promoter regions (P regions), 3′ terminal regions (3′ region), and HPRT1 regions (as control) (Figure 3A). Using three female lines without *XIST* expression (ADSC-iPS, SEES1, and SEES5), we conducted various transfection experiments and assessed the H3K27me3 status.

Seven days after transfection, the HDR approach resulted in the generation of a significantly greater number of H3K27me3+ clones in all three lines compared with that in controls (Figures 3B and 3C). Surprisingly, we found that the NHEJ approach using P region gRNA also resulted in the significant and efficient generation of H3K27me3+ clones (Figures 3B and 3C). Moreover, we did not obtain clones with two H3K27me3 foci (Figure 3B), indicating that XCI with two X chromosomes (Figure 3Aiii) would be harmful to cell viability.

We further determined whether NHEJ-mediated gene reactivation occurs in DNAme-regulated genes other than *XIST*. We found that *GTL2*, an imprinted gene regulated by DNAme (Stadtfeld et al., 2010), was repressed in the BJ- and 2B-iPS lines, whereas SEES3 and SEES6 lines expressing *GTL2* showed DNA hypomethylated states at the regulatory element known as intergenic differentially methylated regions (IG-DMRs) (Figures S3A and S3B). We designed gRNA targeting the IG-DMR (da Rocha et al., 2008) and performed a transfection experiment (Figure S3C). The qPCR assay demonstrated that the *GTL2* expression levels were significantly upregulated in the cells with Cas9/gRNA (IG-DMR) compared with that in control cells in both BJ- and 2B-iPS lines (Figure S3D). The DNAme levels in IG-DMR were reduced in the transfected cells when gRNA targeting IG-DMR was used (Figure S3E). These results indicated that CRISPR-Cas9-mediated NHEJ causes the reactivation of genes repressed by DNAme.

Figure 3. Editing of *XIST* regulatory elements leads to the de-erosion of female hPSCs

(A) Experimental scheme for *XIST* re-expression in eroded female hPSCs. Gene targeting (top panel: HDR approach) and DSB-mediated *XIST* reactivation (bottom panel: NHEJ approach) are shown. For the HDR approach, a large construct (Entire-hXIST) containing the full-length human *XIST* gene was used. The gRNAs were designed at the 5′ promoter regions within exon 1 (P region) and 3′ regions of exon 6 (3′ region). The P region is located between the P1 and P2 promoter regions (Chapman et al., 2014). For the NHEJ approach, the gRNAs of the P region, 3′ region, or HPRT1 region (as negative control) were used, respectively. *XIST*– female hPSC lines were used, and the H3K27me3 statuses were examined to determine whether XCI was reacquired. The three expected XCI patterns are shown [i-iii]. Xi: inactive X chromosome, Xe: eroded X chromosome, and Xa: active X chromosome.

(B and C) Efficiency test of clones with H3K27me3 foci reacquisition in various combinations. Representative images (B) and quantification results (C) are shown on the left and right, respectively. Clones containing at least ten cells with the H3K27me3 foci were counted as positive clones. Each dot and n.c. indicates an independent experiment and the total number of clones counted, respectively. Error bars show the SD. p values were calculated using Student's t test. Scale bar represents 10 μm.

(D and E) RNA-FISH analysis. *XIST*/*XACT*/HUWE1 were examined. Representative images (D) and quantification results (E) are shown in the left and right, respectively. n.c. refers to the number of cells analyzed. Scale bar represents 50 μm.

(F) Expression ratio of X-linked genes in *XIST*+ and *XIST*– female hPSCs based on median levels. The heatmap shows the ratio of X-linked genes (*XIST*–/*XIST*+). The X-linked genes expressed in at least ten cells in both the *XIST*+ and *XIST*– groups were used for the analysis. n refers to the number of X-linked genes analyzed.

(G) Bisulfite sequencing (BS) analysis around the *XIST* promoter region. Differentially methylated regions (DMRs) with approximately 50% of the DNA methylated regions were identified in IMR-90 cells (Roadmap Epigenomics project data). BS and PCR regions in (iii) are shown in green, red, and blue, respectively. (i) and (ii) indicate BS analysis in the SEES5 background (i) and SE-res-5a (ii). (iii) PCR analysis using genomic DNA (gDNA) or cDNA from the SE5-res-5a line.

(H) Summary of XCI-reacquired female hPSCs formed via the editing of *XIST* regulatory regions. After the induction of DSB by Cas9 around the *XIST* promoter regions with DNAme, the cells with XCI reacquired on the Xe allele were naturally selected in a normal culture.

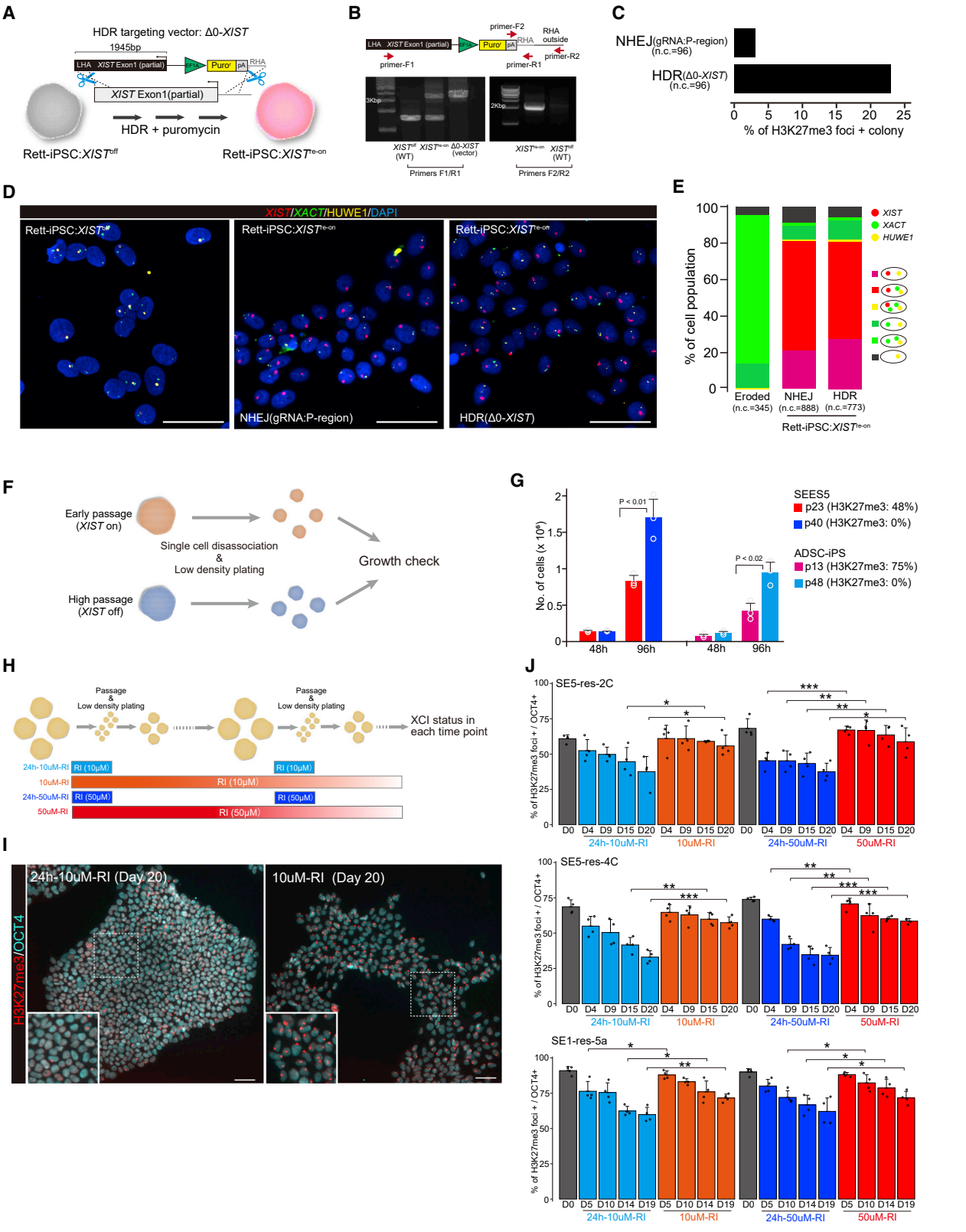

(legend on next page)

Using one of two approaches, we obtained clones with single H3K27me3 foci in >85% of cells, termed SE1-res-5a (SEES1 line), SE5-res-2C (SEES5 line), and SE5-res-4C (SEES5 line). We used the HDR approach for the generation of SE5-res-2C and SE5-res-4C lines. However, using genotyping PCR, we detected the sequences spanning *XIST* and exogenous sequences included in Entire-hXIST vector only in the SE5-res-2C line (Figure S4Ai and S4Aii). Sanger sequencing analysis also confirmed the presence of single-nucleotide variants (SNVs) derived from Entire-hXIST only in SE5-res-2C (Figure S4Aiii). We also confirmed the integration of exogenous sequences derived from at 3′ region of *XIST* in the SE5-res-2C line, but at the 5′ regions of *XIST*, even though we tested several primers spanning the sequences exogenous and upstream of the *XIST* transcription start sites, none of them detected the expected amplicon. Meanwhile, the DNA-FISH experiment using the SE5-res-2C line showed two *XIST*/*XACT* signals, respectively, indicating no additional *XIST* integration (Figure S4B). In terms of *XIST* reactivation in the SE5-res-2C line, recombination occurred in the cells; however, since editing of the P region was sufficient to reactivate *XIST* via NHEJ, we cannot determine if *XIST* reactivation resulted from recombination.

We found scars around the P region in the SE5-res-4C line, but the P region was non-scarred in the SE5-res-2C line (Figure S4C), indicating that H3K27me3 foci reacquisition in SE5-res-4C was mediated by NHEJ; however, we did not exclude the possibility that HDR did not occur in the SE5-res-4C line because the available SNV information is limited. In the SE1-res-5a line, we employed the NHEJ approach, and genotyping PCR analysis around the P region revealed the presence of two alleles with different deletions (Figures S4D and S4E).

Next, we examined whether *XIST* was expressed from an eroded (Figure 3Ai) or active (Figure 3Aii) allele in the three lines. Since *HUWE1* is often protected from erosion and is used as an active allele marker (Motosugi et al., 2021; Patel et al., 2017; Sahakyan et al., 2017), we conducted RNA-FISH analysis using *XIST*, HUWE1, and *XACT*, a marker of eroded hPSCs (Vallot et al., 2015). In the assay, 68%–98% of *XIST*+ cells exhibited monoallelic *XACT* expression, and most of the cells retained HUWE1 expression (Figures 3D and 3E), indicating the occurrence of X-linked gene silencing and expression of *XIST* from the eroded allele (Figure 3Ai). The scRNA-seq analysis also showed that *XIST* reactivation results in the downregulation of X-linked genes (Figure 3F). In these clones, we observed reduced DNAme levels and the expression of *XIST* from an unmethylated allele (Figure 3G), consistent with the findings from a previous report (Fukuda et al., 2021). Taken together, these results demonstrated that XCI erosion can be corrected by *XIST* reactivation with the endogenous transcriptional system, and cells with normal XCI proliferate naturally under normal cultural conditions without specific selection; presumably, normal dosage compensation leads to a growth advantage (Figure 3H).

An efficient HDR-based screening method for *XIST*-reactivated hPSCs and maintenance of *XIST*+ hPSCs

Although the editing of *XIST* P regions by NHEJ or HDR approaches served as a useful tool for *XIST* reactivation, the efficiency of obtaining positive clones for H3K27me3 remained low. In particular, the use of Entire-hXIST (large size >30 kb) resulted in poor survivability after transfection (data not shown). To conduct an easy selection with HDR, we generated a small targeting vector containing the sequences at the *XIST* P regions and a puromycin-resistant gene upstream of the *XIST* transcription start site (Δ0-*XIST*; Figure 4A). To test the practicality of X-linked disease modeling of hiPSCs, we used an hiPSC line derived from a patient with Rett syndrome, which is caused by an X-linked mutation in *MECP2* (Pohodich and Zoghbi, 2015). The Rett-iPSCs showed an absence of H3K27me3 foci, indicating the lack of *XIST* expression (Rett-iPSC:*XIST*^{off}; Figure S4F), and RT-PCR showed the expression from the mutant allele of *MECP2*, indicating that *MECP2* deregulation is protected in this line irrespective of XCI erosion (Figure S4G). Using the Rett-iPSC:*XIST*^{off} line as the parent cell, we obtained the H3K27me3+ clone by puromycin selection and confirmed the heterogeneous clone with the Δ0-*XIST* allele (Figure 4B). The efficiency of the HDR approach using Δ0-*XIST* was more than 7-fold greater than that of the NHEJ approach (Figure 4C). We confirmed that Rett-iPSC lines with *XIST* re-expression (Rett-iPS:*XIST*$^{re\text{-}on}$) maintain HUWE1 monoallelic expression with a normal karyotype (Figures 4D, 4E, and S4H), demonstrating that the use of Δ0-*XIST* for the HDR

Figure 4. An HDR-based efficient screening method for *XIST*-reactivated hPSCs and maintenance of *XIST*+ hPSCs

(A) Scheme of the *XIST* re-expressing line using an Δ0-*XIST* plasmid for HDR. hiPSC line obtained from a patient with Rett syndrome (Rett-iPSCs). Puromycin-resistant gene under the control of the EF1A promoter was inserted upstream of the *XIST* transcription starting site. The transfected cells were treated with puromycin before the H3K27me3 quantification experiment.

(B) Genotyping of Rett-iPSC:*XIST*$^{re\text{-}on}$ line generated byΔ0-*XIST* construct.

(C) Efficiency test of clones with H3K27me3 foci reacquisition. The efficiency of HDR using Δ0-*XIST* plasmid was compared with that of the NHEJ method using P region gRNA. Clones containing at least ten cells with H3K27me3 foci were counted as positive clones. n.c. refers to the number of colonies analyzed.

(D and E) *XIST*/*XACT*/HUWE1 RNA-FISH analysis. The representative images (D) and quantification results (E). n.c. refers to the number of cells analyzed. Scale bar represents 50 μm.

(F) Cell growth test. Cells with different passage numbers (different *XIST* expression statuses) were used for assays. After single-cell dissociation, the cells were cultured, and the viable cells were automatically counted by CountessII (Thermo Fisher Scientific, Waltham, MA, USA) after trypan blue staining at each time point.

(G) Quantification of viable cells. Each dot indicates an independent experiment. Error bars show standard deviations. p values were calculated using Student's t test.

(H) Experimental scheme for maintaining *XIST*+ hPSCs using a Rho-kinase inhibitor (ROCK inhibitor [RI]). The RI inhibitor Y27632 was used transiently or continuously, and the XCI status was examined by immunofluorescence analysis using OCT4 and H3K27me3 at each time point.

(I) Representative image of the H3K27me3/OCT4 status at day 20.

(J) Quantification of the H3K27me3 foci at each time point. Each dot indicates an independent experiment. Error bars show standard deviations. p values were calculated using Student's t test. *$p < 0.05$, **$p < 0.01$, and ***$p < 0.001$. Scale bar represents 50 μm.

approach is the easiest method to generate an *XIST* re-expressed female hPSC line.

Our strategy for *XIST* re-expression by gene editing is useful for the de-erosion of dosage compensation. However, given that DNMT3A/3B is active (Fukuda et al., 2021), the permanent prevention of *XIST* repression is inevitable. Thus, we next sought culture methods to maintain *XIST*+ female hPSCs. We noted that, compared with that observed in eroded female hPSC lines, during conventional culture, female hPSC lines with low passage, often retaining *XIST* expression, showed markedly poor growth after the removal of the Rho-kinase (ROCK) inhibitor Y27632 (Watanabe et al., 2007) (Figures 4F and 4G). We inferred that the presence of the ROCK inhibitor in the culture medium might reduce the loss of *XIST*+ cells. To test this possibility, we cultured the rescued XCI lines in the presence of the ROCK inhibitor Y27632 every day and assessed their XCI statuses (Figure 4H). We found that the daily use of the ROCK inhibitor significantly inhibited the loss of H3K27me3+ cells with OCT4 expression (Figures 4I and 4J). These results indicate that the continuous use of a ROCK inhibitor during culture is beneficial for the maintenance of *XIST*+ female hPSCs.

XCI reacquisition restores differentiation ability

A key question is if XCI reacquisition can rescue the differentiation potential of cells. Since the method for MN differentiation is useful for all studied hPSC lines, we generated MNs using the eroded and rescued XCI lines (Figure 5A). Immuno-FISH analysis showed that in the SEES1 line, the differentiation efficiency of the SE1-res-5a line was comparable to that of the parental eroded line (Figures 5B and 5C), suggesting that XCI is not a major determinant of MN differentiation in the SEES1 line. In contrast, a drastic improvement in the differentiation efficiency was observed in both the SE5-res-2C and -4C lines (>37% of cells) compared with that in the eroded line (3% of cells) (Figures 5B and 5C).

We further investigated whether the differentiation potential of Rett-iPSCs depends on *XIST* expression. Since Rett syndrome affects the CNS (Pohodich and Zoghbi, 2015), we generated cortical organoids in eroded Rett-iPS:*XIST*^{off} and Rett-iPS:*XIST*$^{re\text{-}on}$ by HDR using Δ0-*XIST* (Figure 5A). Surprisingly, immunofluorescence analysis revealed that the Rett-iPS:*XIST*^{off} line showed poor neuronal development, characterized by TUJ-1/ISL1, at day 20 from differentiation (Figures 5D and 5E). In contrast, the Rett-iPS:*XIST*$^{re\text{-}on}$ line exhibited steady neuronal differentiation (Figures 5D and 5E). Considering that neurogenesis is not markedly impaired in hPSCs with MECP2 mutations (Ohashi et al., 2018; Xiang et al., 2020), these results indicated that *XIST* silencing could lead to the misinterpretation of the experimental outcomes in disease iPSCs.

Taken together, erosion of dosage compensation causes underestimation of the intrinsic differentiation abilities of female hPSCs in some genetic backgrounds; however, this can be restored through *XIST* re-expression.

Relation of the *XIST* expression status with cell types *in vivo*

Finally, we focused on the effect of the *XIST* expression status in female cells *in vivo*. Using 61 published scRNA-seq datasets (Han et al., 2020), we first examined if the overexpression of X-linked genes is observed in specific cell types. Considering that the transcriptome status varies among cell types (Han et al., 2020; Thomsen et al., 2016), we focused on cells in the same cluster and further divided the cells into two groups based on *XIST* expression status (Figure S5A). Although we could not determine if the cells without *XIST* expression show lack of *XIST* transcripts, as observed in the RNA-FISH of female hPSCs (Figure 3D), to obtain insights into the X-linked gene-expression status, we calculated the expression ratio of X-linked genes based on the median expression levels between *XIST*+ and *XIST*– cells (Figure S5A). The median levels varied widely in each cluster of various tissues (Figures S5B and S5C), but some clusters, such as cluster 2 in the transverse colon and cluster 3 in the fetal intestine, showed a strong tendency of overexpression in *XIST*– cells (Figures S5B and S5C). Interestingly, *ACE2*, a gene encoding a protein with an important role in severe acute respiratory syndrome coronavirus 2 (SARS-CoV-2) infection (Lan et al., 2020), has been reported to show a heterogeneous expression status *in vivo* (Tukiainen et al., 2017) and is expressed at high levels in intestinal tissues (Figures S5B and S5C). To examine the relation of *ACE2* expression with the *XIST* status, we focused on fetal intestinal and ileal cells (Martin et al., 2019) (Figure S5D). After the identification of the clusters marked by *ACE2* (Figure S5D), we checked the *ACE2* expression levels based on the *XIST* expression status in individual cells. The *ACE2* expression levels in *XIST*– cells tended to be higher than those in *XIST*+ cells, and the differences were statistically significant in some clusters (Figure S5E), suggesting that *XIST* repression might increase the risk of SARS-CoV-2 infection in women.

We further investigated whether *XIST* expression status is linked with neuronal development, such as in *ex vivo* modeling using hPSCs (Figure S2). Using fetal brain tissue datasets, we examined the cell types based on the *XIST* expression status (Figure S5F). Although they were derived at different developmental stages (Han et al., 2020), various cell types, such as radial glial cells and post-mitotic neurons, were identified (Figure S8G). UMAP showed that *XIST* expression was widely distributed (Figure S5G), but the gene was identified as a positive marker in clusters of some excitatory neuron types, such as those with *LHX5-AS1* expression, recently identified in developing brains (Eze et al., 2021) (Figure S5H). We further found that the percentages of neuronal cells tend to be higher among *XIST*+ cells (Figure S5I). In contrast, progenitors were more enriched in *XIST*– cells (Figure S5I). Although the differences in differentiating cell types between *XIST*+ and *XIST*– cells were not remarkable compared with the results obtained from *ex vivo* modeling (Figure S2K), these results suggested that *XIST* repression might affect neuronal differentiation *in vivo*, as observed in hPSC modeling.

DISCUSSION

In the present study, we revealed that *XIST* repression is a key source of noise and one of the chief drivers of variation determining how and if female hPSCs differentiate effectively (Figure 5F). The scRNA-seq data revealed that among female hPSCs, the differentiation scores of *XIST*+ cells tend to be higher than those of *XIST*– cells (Figure 1D), consistent with findings

CellPress
OPEN ACCESS

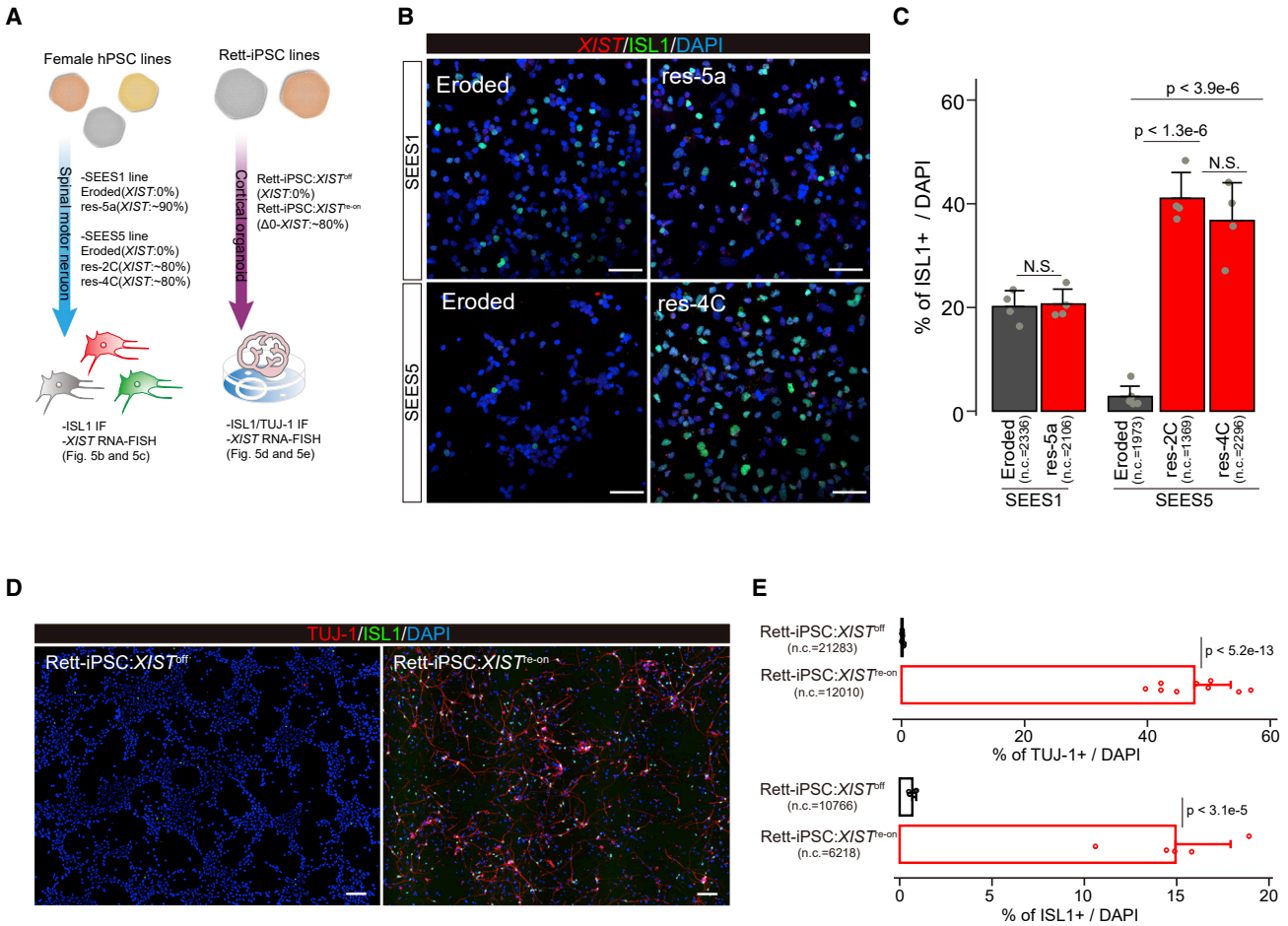

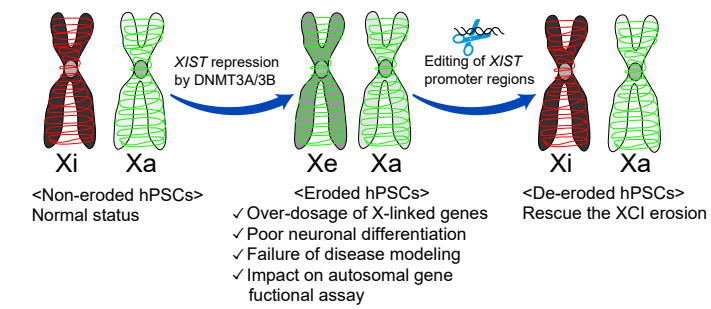

Figure 5. XCI reacquisition restores the differentiation ability of female hPSCs

(A) Experimental schemes for evaluating the differentiation potential by *XIST* repression. *XIST* re-expressing hPSC lines and their parental lines without *XIST* expression were used. Immuno-FISH (for MN) or immunofluorescence (for cortical organoid) analysis was used for the evaluation.

(B and C) The efficiency of MN differentiation from *XIST* re-expressing hPSC lines. The representative images (B) and bar graphs are quantification results for ISL1+ cells (C). Each dot and n.c. indicate the percentage in the observed area and number of cells analyzed in total, respectively. Scale bar represents 50 μm. Error bars show the SD. p values were calculated using Student's t test.

(D and E) The efficiency of neuronal differentiation from Rett-iPSC:*XIST*$^{re\text{-}on}$. The representative images (D) and bar graphs are quantification results of TUJ-1 or ISL1+ cells (E). Each dot and n.c. indicate the percentage in the observed area and number of cells analyzed in total, respectively. Scale bar represents 50 μm. Error bars show the SD. p values were calculated using Student's t test.

(F) Summary of female hPSC erosion and de-erosion. *XIST* is irreversibly repressed by DNMT3A/3B (Fukuda et al., 2021), leading to XCI erosion. XCI erosion affects various phenotypes, not only X-linked gene dysregulation but also the autosomal gene functional assay. *XIST* is reactivated by the editing of *XIST* promoter regions, resulting in the generation of de-eroded hPSCs by natural selection under normal culture conditions.

from previous reports showing that XCI erosion results in a low degree of differentiation into the three germ layers (Anguera et al., 2012; Salomonis et al., 2016). We found that post-mitotic neurons from female hPSCs are enriched in *XIST*+ cells rather than in *XIST*– cells (Figures S2C and S2K), whereas progenitor cells show the opposite pattern (Figures S2C and S2K). Interestingly, a similar tendency was observed in *in vivo* development (Figure S5I). Although the causes leading to the differential differentiation status based on *XIST* expression remain unclear, some possibilities are that *XIST* transcripts might be more accumulated in neurons because they are post-mitotic cells and that overexpression of X-linked genes might be a roadblock in the differentiation of progenitors to neurons.

We also found that in primary and differentiated cells, representative heterochromatin modifications were lost in some cells even when *XIST* was expressed, suggesting that biallelic expression might occur even when *XIST* is expressed. Therefore, the situation of XCI erosion occurring *in vivo* might not be the same as that in female hPSCs.

Since *XIST* reactivation can reduce the side effects of XCI erosion, it is beneficial for the application of female hPSCs in different research areas, including the application of disease iPSCs with mutation in not only X-linked but also autosomal genes. Moreover, the methods can induce gene expression at physiological levels, eliminating the unexpected effects of the artificial transcription system with strong induction.

We also found that daily exposure to the ROCK inhibitor is beneficial for the maintenance of female hPSCs with *XIST* expression. Although the exact mechanisms underlying the development of the phenotype are unknown, the population of early-passage female hPSCs, which occasionally includes *XIST*+ cells, showed slower growth than the eroded lines (Figure 4G), consistent with the findings from a previous report (Anguera et al., 2012). Furthermore, among female hPSCs, the metabolism of cells in non-eroded states differed from that of cells in eroded states (Brenes et al., 2021). These observations indicate that female hPSCs with *XIST* expression might be vulnerable to single-cell dissociation and that the ROCK inhibitor might prevent cell death.

XIST is the only identified lncRNA that acts in *cis* at a chromosomal scale in humans, and its dysregulation affects broad aspects of female cells both *in vitro* and *in vivo*. With dosage compensation, when we revisit inexplicable biological phenomena, we might discover new frontiers in human biology and determine the extent to which phenotypes are attributed to sex differences.

Limitations of the study

Although the *in vivo* scRNA-seq data did not detect *XIST* transcripts, given that these data were not validated by other assays, such as RNA-FISH, and that the scRNA-seq platform used in the study mainly detected the 3′ region of transcripts, we cannot exclude the possibility that *XIST* was not detected because of technical limitations, such as drop-out events in the scRNA-seq analysis and/or low expression levels at the 3′ region.

As for the DNMT3A/3B dKO data, we observed that the *XIST* expression status greatly affected MN differentiation rather than DNMT3A/3B mutations; however, a previous study using male hPSC lines showed that these mutations impaired MN differentiation (Ziller et al., 2018). Thus, the effects of DNMT3A/3B on the differentiation potential of MNs may also depend on the genetic background.

For the SE5-res-2C line, we did not obtain evidence that recombination occurs at the 5′ region of the endogenous *XIST* gene. However, the affinity of the primer sequences used for the genotyping assay toward the genome may have been poor. Therefore, we could not ascertain whether or not the recombination occurred at the 5′ region.

STAR★METHODS

Detailed methods are provided in the online version of this paper and include the following:

- KEY RESOURCES TABLE
- RESOURCE AVAILABILITY
  - Lead contact
  - Materials availability
  - Data and code availability
- EXPERIMENTAL MODEL AND SUBJECT DETAILS
  - Method details
  - Quantification and statistical analysis

SUPPLEMENTAL INFORMATION

Supplemental information can be found online at https://doi.org/10.1016/j.crmeth.2022.100352.

ACKNOWLEDGMENTS

We would like to thank the members of the Support Center for Medical Research and Education, Tokai University School of Medicine, for assisting with the various experiments. The study was supported by AMED under grant numbers JP21bm0704038 and 21bm0804030h0001 to A.F.

AUTHOR CONTRIBUTIONS

A.F. conceptualized the project. A.F., N.M., and A.S. designed the experiments. N.M. and A.S. conducted most of the experiments, with help from A.S., C.O., and A.F. N.M., A.S., C.O., A.O., S.H., and A.F. analyzed the data. N.M., A.S., and A.F. generated cell lines with gene manipulations. A.U. and H.A. generated wild-type ESCs and ADSC-, EDOM-, and BJ-hiPSC lines. All authors interpreted the data, and A.F. supervised the project. A.F. wrote the manuscript with input from all authors.

DECLARATION OF INTERESTS

A.F. is applying for a patent for the method to generate *XIST* re-expressing female hPSCs by gRNA-mediated *XIST* demethylation (2022-062974).

Received: March 18, 2022
Revised: June 29, 2022
Accepted: October 28, 2022
Published: November 29, 2022

REFERENCES

Akutsu, H., Machida, M., Kanzaki, S., Sugawara, T., Ohkura, T., Nakamura, N., Yamazaki-Inoue, M., Miura, T., Vemuri, M.C., Rao, M.S., et al. (2015). Xenogeneic-free defined conditions for derivation and expansion of human embryonic

stem cells with mesenchymal stem cells. Regen. Ther. *1*, 18–29. https://doi.org/10.1016/j.reth.2014.12.004.

An, C., Feng, G., Zhang, J., Cao, S., Wang, Y., Wang, N., Lu, F., Zhou, Q., and Wang, H. (2020). Overcoming autocrine FGF signaling-induced heterogeneity in naive human ESCs enables modeling of random X chromosome inactivation. Cell Stem Cell *27*, 482–497.e84. https://doi.org/10.1016/j.stem.2020.06.002.

Anguera, M.C., Sadreyev, R., Zhang, Z., Szanto, A., Payer, B., Sheridan, S.D., Kwok, S., Haggarty, S.J., Sur, M., Alvarez, J., et al. (2012). Molecular signatures of human induced pluripotent stem cells highlight sex differences and cancer genes. Cell Stem Cell *11*, 75–90. https://doi.org/10.1016/j.stem.2012.03.008.

Augui, S., Nora, E.P., and Heard, E. (2011). Regulation of X-chromosome inactivation by the X-inactivation centre. Nat. Rev. Genet. *12*, 429–442. https://doi.org/10.1038/nrg2987.

Bhaduri, A., Andrews, M.G., Mancia Leon, W., Jung, D., Shin, D., Allen, D., Jung, D., Schmunk, G., Haeussler, M., Salma, J., et al. (2020). Cell stress in cortical organoids impairs molecular subtype specification. Nature *578*, 142–148. https://doi.org/10.1038/s41586-020-1962-0.

Bock, C., Kiskinis, E., Verstappen, G., Gu, H., Boulting, G., Smith, Z.D., Ziller, M., Croft, G.F., Amoroso, M.W., Oakley, D.H., et al. (2011). Reference Maps of human ES and iPS cell variation enable high-throughput characterization of pluripotent cell lines. Cell *144*, 439–452. https://doi.org/10.1016/j.cell.2010.12.032.

Brenes, A.J., Yoshikawa, H., Bensaddek, D., Mirauta, B., Seaton, D., Hukelmann, J.L., Jiang, H., Stegle, O., and Lamond, A.I. (2021). Erosion of human X chromosome inactivation causes major remodeling of the iPSC proteome. Cell Rep. *35*, 109032. https://doi.org/10.1016/j.celrep.2021.109032.

Cali, C.P., Park, D.S., and Lee, E.B. (2019). Targeted DNA methylation of neurodegenerative disease genes via homology directed repair. Nucleic Acids Res. *47*, 11609–11622. https://doi.org/10.1093/nar/gkz979.

Cao, J., Spielmann, M., Qiu, X., Huang, X., Ibrahim, D.M., Hill, A.J., Zhang, F., Mundlos, S., Christiansen, L., Steemers, F.J., et al. (2019). The single-cell transcriptional landscape of mammalian organogenesis. Nature *566*, 496–502. https://doi.org/10.1038/s41586-019-0969-x.

Chapman, A.G., Cotton, A.M., Kelsey, A.D., and Brown, C.J. (2014). Differentially methylated CpG island within human XIST mediates alternative P2 transcription and YY1 binding. BMC Genet. *15*, 89. https://doi.org/10.1186/s12863-014-0089-4.

Clemson, C.M., McNeil, J.A., Willard, H.F., and Lawrence, J.B. (1996). XIST RNA paints the inactive X chromosome at interphase: evidence for a novel RNA involved in nuclear/chromosome structure. J. Cell Biol. *132*, 259–275. https://doi.org/10.1083/jcb.132.3.259.

da Rocha, S.T., Edwards, C.A., Ito, M., Ogata, T., and Ferguson-Smith, A.C. (2008). Genomic imprinting at the mammalian Dlk1-Dio3 domain. Trends Genet. *24*, 306–316. https://doi.org/10.1016/j.tig.2008.03.011.

Doudna, J.A., and Charpentier, E. (2014). Genome editing. The new Frontier of genome engineering with CRISPR-Cas9. Science *346*, 1258096. https://doi.org/10.1126/science.1258096.

Eze, U.C., Bhaduri, A., Haeussler, M., Nowakowski, T.J., and Kriegstein, A.R. (2021). Single-cell atlas of early human brain development highlights heterogeneity of human neuroepithelial cells and early radial glia. Nat. Neurosci. *24*, 584–594. https://doi.org/10.1038/s41593-020-00794-1.

Fukuda, A., Hazelbaker, D.Z., Motosugi, N., Hao, J., Limone, F., Beccard, A., Mazzucato, P., Messana, A., Okada, C., San Juan, I.G., et al. (2021). De novo DNA methyltransferases DNMT3A and DNMT3B are essential for XIST silencing for erosion of dosage compensation in pluripotent stem cells. Stem Cell Rep. *16*, 2138–2148. https://doi.org/10.1016/j.stemcr.2021.07.015.

Fukuda, A., Mitani, A., Miyashita, T., Sado, T., Umezawa, A., and Akutsu, H. (2016). Maintenance of Xist imprinting depends on chromatin condensation state and Rnf12 dosage in mice. PLoS Genet. *12*, e1006375. https://doi.org/10.1371/journal.pgen.1006375.

Guo, G., von Meyenn, F., Rostovskaya, M., Clarke, J., Dietmann, S., Baker, D., Sahakyan, A., Myers, S., Bertone, P., Reik, W., et al. (2017). Epigenetic resetting of human pluripotency. Development *144*, 2748–2763. https://doi.org/10.1242/dev.146811.

Han, X., Zhou, Z., Fei, L., Sun, H., Wang, R., Chen, Y., Chen, H., Wang, J., Tang, H., Ge, W., et al. (2020). Construction of a human cell landscape at single-cell level. Nature *581*, 303–309. https://doi.org/10.1038/s41586-020-2157-4.

Hao, Y., Hao, S., Andersen-Nissen, E., Mauck, W.M., 3rd, Zheng, S., Butler, A., Lee, M.J., Wilk, A.J., Darby, C., Zager, M., et al. (2021). Integrated analysis of multimodal single-cell data. Cell *184*, 3573–3587.e29. https://doi.org/10.1016/j.cell.2021.04.048.

Klim, J.R., Williams, L.A., Limone, F., Guerra San Juan, I., Davis-Dusenbery, B.N., Mordes, D.A., Burberry, A., Steinbaugh, M.J., Gamage, K.K., Kirchner, R., et al. (2019). ALS-implicated protein TDP-43 sustains levels of STMN2, a mediator of motor neuron growth and repair. Nat. Neurosci. *22*, 167–179. https://doi.org/10.1038/s41593-018-0300-4.

Lan, J., Ge, J., Yu, J., Shan, S., Zhou, H., Fan, S., Zhang, Q., Shi, X., Wang, Q., Zhang, L., and Wang, X. (2020). Structure of the SARS-CoV-2 spike receptor-binding domain bound to the ACE2 receptor. Nature *581*, 215–220. https://doi.org/10.1038/s41586-020-2180-5.

Liao, J., Karnik, R., Gu, H., Ziller, M.J., Clement, K., Tsankov, A.M., Akopian, V., Gifford, C.A., Donaghey, J., Galonska, C., et al. (2015). Targeted disruption of DNMT1, DNMT3A and DNMT3B in human embryonic stem cells. Nat. Genet. *47*, 469–478. https://doi.org/10.1038/ng.3258.

Martin, J.C., Chang, C., Boschetti, G., Ungaro, R., Giri, M., Grout, J.A., Gettler, K., Chuang, L.S., Nayar, S., Greenstein, A.J., et al. (2019). Single-cell analysis of Crohn's disease lesions identifies a pathogenic cellular module associated with resistance to anti-TNF therapy. Cell *178*, 1493–1508.e20. https://doi.org/10.1016/j.cell.2019.08.008.

McCarthy, D.J., Chen, Y., and Smyth, G.K. (2012). Differential expression analysis of multifactor RNA-Seq experiments with respect to biological variation. Nucleic Acids Res. *40*, 4288–4297. https://doi.org/10.1093/nar/gks042.

Mekhoubad, S., Bock, C., de Boer, A.S., Kiskinis, E., Meissner, A., and Eggan, K. (2012). Erosion of dosage compensation impacts human iPSC disease modeling. Cell Stem Cell *10*, 595–609. https://doi.org/10.1016/j.stem.2012.02.014.

Motosugi, N., Okada, C., Sugiyama, A., Kawasaki, T., Kimura, M., Shiina, T., Umezawa, A., Akutsu, H., and Fukuda, A. (2021). Deletion of lncRNA XACT does not change expression dosage of X-linked genes, but affects differentiation potential in hPSCs. Cell Rep. *35*, 109222. https://doi.org/10.1016/j.celrep.2021.109222.

Ohashi, M., Korsakova, E., Allen, D., Lee, P., Fu, K., Vargas, B.S., Cinkornpumin, J., Salas, C., Park, J.C., Germanguz, I., et al. (2018). Loss of MECP2 leads to activation of P53 and neuronal senescence. Stem Cell Rep. *10*, 1453–1463. https://doi.org/10.1016/j.stemcr.2018.04.001.

Patel, S., Bonora, G., Sahakyan, A., Kim, R., Chronis, C., Langerman, J., Fitz-Gibbon, S., Rubbi, L., Skelton, R.J.P., Ardehali, R., et al. (2017). Human embryonic stem cells do not change their X inactivation status during differentiation. Cell Rep. *18*, 54–67. https://doi.org/10.1016/j.celrep.2016.11.054.

Penny, G.D., Kay, G.F., Sheardown, S.A., Rastan, S., and Brockdorff, N. (1996). Requirement for Xist in X chromosome inactivation. Nature *379*, 131–137. https://doi.org/10.1038/379131a0.

Perez-Pinera, P., Kocak, D.D., Vockley, C.M., et al. (2013). RNA-guided gene activation by CRISPR-Cas9-based transcription factors. Nat. Methods *10*, 973–976. https://doi.org/10.1038/nmeth.2600.

Pohodich, A.E., and Zoghbi, H.Y. (2015). Rett syndrome: disruption of epigenetic control of postnatal neurological functions. Hum. Mol. Genet. *24*, R10–R16. https://doi.org/10.1093/hmg/ddv217.

Saarimäki-Vire, J., Balboa, D., Russell, M.A., et al. (2017). An Activating STAT3 Mutation Causes Neonatal Diabetes through Premature Induction of Pancreatic Differentiation. Cell Rep. *19*, 281–294. https://doi.org/10.1016/j.celrep.2017.03.055.

Saelens, W., Cannoodt, R., and Saeys, Y. (2018). A comprehensive evaluation of module detection methods for gene expression data. Nat. Commun. *9*, 1090. https://doi.org/10.1038/s41467-018-03424-4.

Sahakyan, A., Kim, R., Chronis, C., Sabri, S., Bonora, G., Theunissen, T.W., Kuoy, E., Langerman, J., Clark, A.T., Jaenisch, R., and Plath, K. (2017). Human naive pluripotent stem cells model X chromosome dampening and X inactivation. Cell Stem Cell *20*, 87–101. https://doi.org/10.1016/j.stem.2016.10.006.

Salomonis, N., Dexheimer, P.J., Omberg, L., Schroll, R., Bush, S., Huo, J., Schriml, L., Ho Sui, S., Keddache, M., Mayhew, C., et al. (2016). Integrated genomic analysis of diverse induced pluripotent stem cells from the progenitor cell biology consortium. Stem Cell Rep. *7*, 110–125. https://doi.org/10.1016/j.stemcr.2016.05.006.

Shi, T.T., Yang, F.Y., Liu, C., Cao, X., Lu, J., Zhang, X.L., Yuan, M.X., Chen, C., and Yang, J.K. (2018). Angiotensin-converting enzyme 2 regulates mitochondrial function in pancreatic beta-cells. Biochem. Biophys. Res. Commun. *495*, 860–866. https://doi.org/10.1016/j.bbrc.2017.11.055.

Stadtfeld, M., Apostolou, E., Akutsu, H., Fukuda, A., Follett, P., Natesan, S., Kono, T., Shioda, T., and Hochedlinger, K. (2010). Aberrant silencing of imprinted genes on chromosome 12qF1 in mouse induced pluripotent stem cells. Nature *465*, 175–181. https://doi.org/10.1038/nature09017.

Stuart, T., Butler, A., Hoffman, P., Hafemeister, C., Papalexi, E., Mauck, W.M., 3rd, Hao, Y., Stoeckius, M., Smibert, P., and Satija, R. (2019). Comprehensive integration of single-cell data. Cell *177*, 1888–1902.e21. https://doi.org/10.1016/j.cell.2019.05.031.

Takahashi, K., Tanabe, K., Ohnuki, M., Narita, M., Ichisaka, T., Tomoda, K., and Yamanaka, S. (2007). Induction of pluripotent stem cells from adult human fibroblasts by defined factors. Cell *131*, 861–872. https://doi.org/10.1016/j.cell.2007.11.019.

Tan, S.M., Wang, S.T., Hentze, H., and Dröge, P. (2007). A UTF1-based selection system for stable homogeneously pluripotent human embryonic stem cell cultures. Nucleic Acids Res. *35*, e118. https://doi.org/10.1093/nar/gkm704.

Thomsen, E.R., Mich, J.K., Yao, Z., Hodge, R.D., Doyle, A.M., Jang, S., Shehata, S.I., Nelson, A.M., Shapovalova, N.V., Levi, B.P., and Ramanathan, S. (2016). Fixed single-cell transcriptomic characterization of human radial glial diversity. Nat. Methods *13*, 87–93. https://doi.org/10.1038/nmeth.3629.

Thomson, J.A., Itskovitz-Eldor, J., Shapiro, S.S., Waknitz, M.A., Swiergiel, J.J., Marshall, V.S., and Jones, J.M. (1998). Embryonic stem cell lines derived from human blastocysts. Science *282*, 1145–1147.

Tukiainen, T., Villani, A.C., Yen, A., Rivas, M.A., Marshall, J.L., Satija, R., Aguirre, M., Gauthier, L., Fleharty, M., Kirby, A., et al. (2017). Landscape of X chromosome inactivation across human tissues. Nature *550*, 244–248. https://doi.org/10.1038/nature24265.

Vallot, C., Ouimette, J.F., Makhlouf, M., Féraud, O., Pontis, J., Côme, J., Martinat, C., Bennaceur-Griscelli, A., Lalande, M., and Rougeulle, C. (2015). Erosion of X Chromosome inactivation in human pluripotent cells initiates with XACT coating and depends on a specific heterochromatin landscape. Cell Stem Cell *16*, 533–546. https://doi.org/10.1016/j.stem.2015.03.016.

Velasco, S., Kedaigle, A.J., Simmons, S.K., Nash, A., Rocha, M., Quadrato, G., Paulsen, B., Nguyen, L., Adiconis, X., Regev, A., et al. (2019). Individual brain organoids reproducibly form cell diversity of the human cerebral cortex. Nature *570*, 523–527. https://doi.org/10.1038/s41586-019-1289-x.

Wang, Z., Oron, E., Nelson, B., Razis, S., and Ivanova, N. (2012). Distinct lineage specification roles for NANOG, OCT4, and SOX2 in human embryonic stem cells. Cell Stem Cell *10*, 440–454. https://doi.org/10.1016/j.stem.2012.02.016.

Watanabe, K., Ueno, M., Kamiya, D., Nishiyama, A., Matsumura, M., Wataya, T., Takahashi, J.B., Nishikawa, S.i., Nishikawa, S., Muguruma, K., and Sasai, Y. (2007). A ROCK inhibitor permits survival of dissociated human embryonic stem cells. Nat. Biotechnol. *25*, 681–686. https://doi.org/10.1038/nbt1310.

Xiang, Y., Tanaka, Y., Patterson, B., Hwang, S.M., Hysolli, E., Cakir, B., Kim, K.Y., Wang, W., Kang, Y.J., Clement, E.M., et al. (2020). Dysregulation of BRD4 function underlies the functional abnormalities of MeCP2 mutant neurons. Mol. Cell *79*, 84–98.e9. https://doi.org/10.1016/j.molcel.2020.05.016.

Yamanaka, S. (2020). Pluripotent stem cell-based cell therapy-promise and challenges. Cell Stem Cell *27*, 523–531. https://doi.org/10.1016/j.stem.2020.09.014.

Ziller, M.J., Ortega, J.A., Quinlan, K.A., Santos, D.P., Gu, H., Martin, E.J., Galonska, C., Pop, R., Maidl, S., Di Pardo, A., et al. (2018). Dissecting the functional consequences of de novo DNA methylation dynamics in human motor neuron differentiation and physiology. Cell Stem Cell *22*, 559–574.e9. https://doi.org/10.1016/j.stem.2018.02.012.

STAR★METHODS

KEY RESOURCES TABLE

REAGENT or RESOURCE	SOURCE	IDENTIFIER
Antibodies		
Rabbit monoclonal anti-ISL1	Abcam	Cat# ab109517; RRID: AB_10866454
Rabbit monoclonal anti-PAX6	Abcam	Cat# ab195045; RRID: AB_2750924
Mouse monoclonal anti-SATB2	Abcam	Cat# ab51502; RRID: AB_882455
Rat monoclonal anti-Ctip2	Abcam	Cat# ab18465; RRID: AB_2064130
Rabbit monoclonal anti-TBR1	Abcam	Cat# ab183032; RRID: AB_2313773
Mouse monoclonal anti-β3-Tubulin	Cell Signaling Technology	Cat# 4466; RRID: AB_1904176
Mouse monoclonal anti-Oct-3/4 (C-10)	Santa Cruz Biotechnology	Cat# sc-5279; RRID: AB_628051
Rabbit monoclonal anti-H3K27me3	Cell Signaling Technology	Cat# 9733; RRID: AB_2616029
Rabbit polyclonal anti-Dnmt3b	Abcam	Cat# ab16049; RRID: AB_443299
Rabbit polyclonal anti-Dnmt3a	Cell Signaling Technology	Cat# 2160S; RRID: AB_2263617
Rabbit monoclonal anti-GAPDH	Cell Signaling Technology	Cat# 2118; RRID: AB_561053
Chemicals, peptides, and recombinant proteins		
StemFlex	Thermo Fisher Scientific	Cat# A3349401
Matrigel	Corning, Inc	Cat# 354277
Y-27632	Stemcell Technologies	Cat# ST-72308
Neurobasal medium	Thermo Fisher Scientific	Cat# 21103049
B-27 supplement	Thermo Fisher Scientific	Cat# 17504044
N-2 supplement	Thermo Fisher Scientific	Cat# 17502048
GlutaMAX	Thermo Fisher Scientific	Cat# 35050061
SB431542	Stemcell Technologies	Cat# ST-72234
retinoic acid	Stemcell Technologies	Cat# R2625
LDN-193189	Stemcell Technologies	Cat# ST-72147
Smoothend agonist	Stemcell Technologies	Cat# ST-73412
DAPT	Stemcell Technologies	Cat# ST-72082
SU-5402	Stemcell Technologies	Cat# ST-73914
STEMdiff Cerebral Organoid Kit	Stemcell Technologies	Cat# ST-08570
Accutase	Stemcell Technologies	Cat# ST-07920
Neural Tissue Dissociation kit (P)	Miltenyi Biotec	Cat# 130-092-628
Poly-D-Lysine	Thermo Fisher Scientific	Cat# A3890401
VECTASHIELD with DAPI	VECTOR LABORATORIES	Cat# H-1200
RIPA lysis and extraction buffer	Thermo Fisher Scientific	Cat# 89900
Critical commercial assays		
Nick translation kit	Abbott	Cat# 32-801300
EZ DNA Methylation Kit	Zymo Research	Cat# D5001
RNeasy plus micro kit	Qiagen	Cat# 74034
pGEM -T Easy Vector System	Promega	Cat# A137A

(*Continued on next page*)

Continued

REAGENT or RESOURCE	SOURCE	IDENTIFIER
PUC118 cloning vector	Takara Bio Inc.	Cat# 3324
HiFi DNA assembly cloning kit	New England Biolabs	Cat# E2621
Deposited data		
Raw and processed data	This paper	GEO: GSE186128
human cell landscape dataset	Han et al., 2020	GEO: GSE134355
ileal uninvolved tissue samples	Martin et al., 2019	GEO: GSE134809
cortical organoid dataset from the HUES66 line	Broad Institute	portals.broadinstitute.org/single_cell/study/reproducible-brain-organoids
Gene expression data in scRNA-seq.	Mendeley	https://doi.org/10.17632/s3yyxhczs3.1
Experimental models: Cell lines		
Human: female ES cells; SEES1, SEES2, SEES4, SEES5 and SEES7	National Center for Child Health and Development	N/A
Human: female iPS cells; ADSC and EDOM	National Center for Child Health and Development	N/A
Human: male ES cells; SEES3 and SEES6	National Center for Child Health and Development	N/A
Human: male iPS cell; BJ	National Center for Child Health and Development	N/A
Human: male iPS cell; 2B	RIKEN BRC	HiPS-RIKEN-2B
Human: female Rett-iPS cell; HPS3049	RIKEN BRC	HPS3049
Human: DNMT3A/3B double-mutant knockout (dKO) line from SEES5	This paper	N/A
Human: *XIST*-reactivate lines from SEES1, SEES5, ADSC and HPS3049	This paper	N/A
Human: *GTL2*-reactivate lines from BJ and 2B	This paper	N/A
Human: EDOM; female primary cells	National Center for Child Health and Development	N/A
Oligonucleotides		
Primers for TIDE5′, Genotyping, BS and qPCR see Table S2	This paper	N/A
gRNAs of Target region see Table S2	This paper	N/A
Recombinant DNA		
CAG-Cas9-T2A-EGFP-ires-puro	Saarimäki-Vire et al., 2017	Addgene, #78311
pSPgRNA	Perez-Pinera et al., 2013	Addgene, #47108
G1A, Plasmid for human XIST	Clemson et al., 1996	Addgene, #24690; GenBank: NG_016172
BAC clone: human XACT	Thermo Fisher Scientific	CTD 3063K22
BAC clone: human HUWE1	Thermo Fisher Scientific	PR11-975N19
Software and algorithms		
Benchling	Benchling	https://benchling.com; RRID:SCR_013955
TIDE	Bas van Steensel lab.	http://shinyapps.datacurators.nl/tide/
QUMA	RIKEN	http://quma.cdb.riken.jp/
R	R Development Core Team	https://cran.r-project.org
Seurat package (version 3 or 4)	Hao et al., 2021	https://satijalab.org/seurat/
UCSC genome browser	UCSC Genome Bioinformatics Group	https://genome.ucsc.edu/; RRID:SCR_005780
Monocle3	Cao et al., 2019	https://cole-trapnell-lab.github.io/monocle3/; RRID:SCR_018685
edgeR package	McCarthy et al., 2012	https://bioconductor.org/packages/release/bioc/html/edgeR.html; RRID:SCR_012802

RESOURCE AVAILABILITY

Lead contact

Further information and requests for resources should be directed to and will be fulfilled by the lead contact, Atsushi Fukuda (fa972942@tsc.u-tokai.ac.jp).

Materials availability

This study did not generate new unique reagents.

Data and code availability

- Bulk RNA-seq and Single-cell RNA-seq data used in this study have been deposited at GEO and are publicly available. The gene expression data in scRNA-seq have been deposited at Mendeley and the DOI is listed in the key resources table and are publicly available as of the date of publication. Original western blot images have been shown in the figure. Microscopy data reported in this paper will be shared by the lead contact upon request.
- This paper does not report the original code.
- Any additional information required to reanalyze the data reported in this paper is available from the lead contact upon request.

EXPERIMENTAL MODEL AND SUBJECT DETAILS

All human ES cell lines in this study were used under the instruction on the use of human embryonic stem cell research guidelines of Tokai University, the National Center for Child Health and Development, and the Ministry of Education in Japan, and the cell lines used in this study were reported previously (Motosugi et al., 2021). The experiments on X-linked disease iPSCs were approved by the Institutional Review Board for Clinical Research, Tokai University.

Method details

hPSC culture

hPSCs were cultured in StemFlex (Thermo Fisher Scientific, Waltham, MA, USA) on a plate coated with hES cell-grade Matrigel (Corning Inc., Corning, NY, USA). For passaging hPSCs, 1 mM EDTA and 10 μM Y-27632 (StemCell Technologies, Vancouver, Canada) were added to the culture medium and maintained for 24 h, unless otherwise specified. We obtained Rett-iPSCs from the RIKEN bioresource center (HPS3049), and the hPSCs were cultured as described above. The normal chromosome status was confirmed previously (Akutsu et al., 2015). In high passage states, karyotype analysis using G-band staining was performed at Hokkaido Chromosome Science Laboratories, Hokkaido, Japan. Chromosomes were classified according to the International System for Human Cytogenetic Nomenclature. At least 20 metaphase chromosomes were analyzed per cell line.

MN differentiation

Spinal MN differentiation was performed based on methods described in previous reports (Klim et al., 2019; Motosugi et al., 2021). Briefly, the culture medium for confluent hPSCs was replaced with an MN induction medium. The differentiation medium contained ½ Neurobasal (Thermo Fisher Scientific) and ½ DMEM-F12 (Thermo Fisher Scientific) supplemented with Gibco B-27 supplement (×1; Thermo Fisher Scientific), Gibco N-2 supplement (×1; Thermo Fisher Scientific), Gibco GlutaMAX (×1; Thermo Fisher Scientific), and 100 μM non-essential amino acids. The time point at which the medium was changed was defined as day 0 of MN differentiation. We used the following small molecules: 10 μM SB431542 (StemCell Technologies), 1 μM retinoic acid (StemCell Technologies), 100 nM LDN-193189 (StemCell Technologies), and 1 μM Smoothened agonist (StemCell Technologies) on days 0–5; and 5 μM DAPT (StemCell Technologies), 4 μM SU-5402 (StemCell Technologies), 1 μM retinoic acid (StemCell Technologies), and 1 μM Smoothened agonist (StemCell Technologies) on days 6–14. On days 10 or 14, the differentiation efficiency of MNs was analyzed using immuno-FISH analysis. All cells, except naïve cells, were cultured at 37°C in the presence of 5% CO_2.

Generation of cortical organoids

To generate cortical organoids from hPSCs, we used a cerebral organoid differentiation medium (STEMdiff Cerebral Organoid Kit, #08570; StemCell Technologies), in accordance with the manufacturer's instructions. Approximately 70% of the confluent hPSCs were dissociated into single cells using Accutase (#ST-07920; StemCell Technologies), and 9,000 cells were plated in a 96-well plate with ultra-low attachment (#7007; Corning Inc.) and cultured for 5 days. On day 5, the embryoid bodies (EBs) were transferred to a 24-well plate with ultra-low attachment (#3473; Corning Inc.) in 500 μL of neural induction medium. After 48 h, the EBs were embedded in Matrigel and incubated for 30 min at 37°C in a CO_2 incubator to allow the Matrigel to polymerize. After polymerization, 1 mL of expansion medium was added to each well. On day 10, the medium was replaced with 1 mL of maturation medium, and the culture plate was placed in a shaker at 37°C in a CO_2 incubator. The maturation medium was replaced every 3–4 days until further analysis.

Immunofluorescence analysis

Immunofluorescence analysis was performed as previously described (Fukuda et al., 2021; Motosugi et al., 2021). Briefly, the cells were fixed with 4% paraformaldehyde (PFA) in phosphate-buffered saline (PBS) for 20 min. The samples were permeabilized using

0.1% Triton-X for 20 min. After washing with PBS, the samples were blocked with 1.5% bovine serum albumin (BSA) in PBS for 1 h and then subjected to the first antibody reaction. After washing with PBS, the samples were subjected to the second antibody reaction and used for microscopy analysis. Images were captured using an LSM770 microscope (Carl Zeiss, Oberkochen, Germany) or an Axio Imager 2 microscope (Carl Zeiss).

For the analysis of organoids developed from Rett-iPSCs, the organoids were dissociated using Neural Tissue Dissociation Kit (P) (Miltenyi Biotec) in accordance with manufacturer's instruction and plated on a coverslip coated with poly-d-lysine (Thermo Fisher Scientific). After 24 h, the cells were fixed and subjected to immunofluorescence analysis, as described above. Detailed information on the antibodies used in this study is provided in Table S2.

RNA-FISH

Based on previous reports, RNA-FISH was performed as described previously (Fukuda et al., 2021; Motosugi et al., 2021). Briefly, the cells were cultured on a coverslip and fixed by treating with 4% PFA in PBS for 20 min. The samples were permeabilized using 0.1% Triton-X for 20 min and then subjected to RNA-FISH. The probes were prepared using a nick translation kit (Abbott Laboratories, Chicago, IL, USA), with G1A (#24690; Addgene, Cambridge, MA, USA) for *XIST*, and the BAC clones CTD 3063K22 and PR11-975N19 for *XACT* and *HUWE1*, respectively. VECTASHIELD with DAPI was used for nuclear staining (Vector Laboratories Inc., Burlingame, CA, USA). Images were acquired using an LSM770 microscope (Carl Zeiss) or an Axio Imager 2 microscope (Carl Zeiss).

Immunofluorescence analysis combined with RNA-FISH (Immuno-FISH)

Immuno-FISH analysis was conducted based on a method described in a previous report (Fukuda et al., 2021; Motosugi et al., 2021). Briefly, differentiating cells in a 2D culture were detached with Accutase (StemCell Technologies) and plated on a coverslip coated with Matrigel (Corning Inc.) for at least 1 h. After confirming the attachment of the cells under the microscope, the cells were fixed and permeabilized as described above. For immuno-FISH, nuclease-free BSA was used as the blocking buffer and for first antibody incubation. After secondary antibody treatment, the samples were subjected to post-fixation with 4% PFA in PBS for 20 min before *XIST* RNA-FISH. VECTASHIELD with DAPI was used for nuclear staining (Vector Laboratories Inc.).

On day 90, the cortical organoids were fixed overnight in 4% PFA. They were then washed in PBS and transferred to a 10%, 15%, or 20% sucrose solution every 24 h at 4°C. Subsequently, they were transferred into an embedding medium (Tissue-Tek OCT Compound 4583; Sakura Finetek Japan, Tokyo, Japan), frozen using an ultra-low-temperature freezing system (Histo-Tek PINO; Sakura Finetek Japan), and stored at −80°C. For immunohistochemistry, 5 μm-thick sections were obtained using a cryostat, and the specimens were placed onto glass slides and subjected to immuno-FISH, as described above. On day 90, the organoids were analyzed using immuno-FISH. Images were captured using an LSM700 microscope (Carl Zeiss) or an Axio Imager 2 microscope (Carl Zeiss).

DNA-FISH

The DNA-FISH procedures were based on a previous study (Fukuda et al., 2016). The fixed and permeabilised cells were treated with RNaseA and then incubated with 0.2N HCl containing 0.05% tween-20 solution on ice for 10 min. The samples were incubated at 85°C for 10 min and then for overnight at 37°C. Entire-hXIST and CTD 3063K22 were prepared by nick translation. Images were captured using an LSM700 microscope (Carl Zeiss).

Generation of XIST re-expressing female hPSC lines

For the *XIST* re-expression efficiency test, SEES1, SEES5, and ADSC-hiPSC lines (all of them containing >99% of cells without the H3K27me3 foci) were used. The *XIST* re-expressing SEES1 and SEES5 cell lines were used. For the gene targeting approach in *XIST* re-expression experiments, using bacterial recombineering technology, we generated a Targeting vector containing the whole human *XIST* gene (32 kb): Entire-hXIST contains exogenous sequences of a tetracycline response element upstream of the *XIST* transcription starting site and a SV40 polyA signal downstream of the *XIST* gene (Vector Builder, Chicago, IL, USA). Entire-hXIST was used for the transfection experiments. To induce recombination, Entire-hXIST was co-transfected with CAG-Cas9-T2A-EGFP-ires-puro (a gift from Timo Otonkoski, #78311; Addgene) and pSPgRNA (a gift from Charles Gersbach, #47108; Addgene). The gRNAs were designed to target the promoter (P-region) and 3′ regions of *XIST*. For the gRNA-mediated *XIST* or *GTL2* reactivation experiments, CAG-Cas9-T2A-EGFP-ires-puro and pSPgRNA containing each target sequence were co-transfected. The gRNA sequences used in this study are listed in Table S2. For the *GTL2* re-expression experiments, BJ- and 2B-hiPSC lines were used. The gRNAs were designed using Benchling (https://benchling.com).

At 24 h after transfection, 1.5–2 μg of puromycin (depending on the cell line used) was added to the culture medium and maintained for 24 h. Then, each colony was subjected to immunofluorescence staining against H3K27me3 to evaluate the efficiency of XCI reacquisition or sub-cloning into 96-well plates. After sub-cloning, we screened H3K27me3-positive clones (>85% of cells in each population).

For the generation of the Rett-iPSC: $XIST^{re\text{-}on}$ line, the Δ0-*XIST* plasmid was constructed using HiFi DNA assembly according to the manufacturer's instruction (NEB). PUC118-HindIII (#3324; Takara Bio Inc., Siga, Japan) was used as a backbone plasmid. All fragments were generated by PCR using Entire-hXIST and genomic DNA, and original plasmids contained EF1a promoter sequences (available upon request). A part of Exon 1 in the *XIST* gene and upstream regions from TSS was used for the targeting arms. The gRNAs were generated as described above, and the sequences are listed in Table S2. After transfection, Rett-iPSCs were cultured till approximately 70% confluence was achieved and were then subjected to puromycin selection.

Generation of DNMT3A/3B double-mutant lines

The previously validated gRNAs for DNMT3A or 3B and the SEES5 line with or without *XIST* expression were used (Fukuda et al., 2021; Liao et al., 2015). gRNA was cloned into pSPgRNA, and two gRNAs targeting DNMT3A and 3B were co-transfected with

CAG-Cas9-T2A-EGFP-ires-puro. The screening method is described above; the mutations were identified by genomic PCR, and deletion was confirmed by western blotting analysis.

Genotyping

XIST re-expressing hPSC lines were subjected to genomic PCR using primers spanning exogenous sequences when they were generated using TRE-hXIST. To check for scars in each gene editing scenario, TIDE (http://shinyapps.datacurators.nl/tide/) analysis was conducted around the gRNA targeting sequences. For Rett-iPSCs, the mutant region reported in the RIKEN bioresource center was confirmed by PCR and Sanger sequencing. All primer sequences are listed in Table S2.

Western blotting

Western blotting was performed using the conventional method (Fukuda et al., 2021; Liao et al., 2015). Briefly, proteins from hPSCs were extracted using RIPA lysis and extraction buffer (Thermo Fisher Scientific). The extracted proteins were subjected to sodium dodecyl sulfate-polyacrylamide gel electrophoresis using 7.5% TGX gel (Bio-Rad, Hercules, CA, USA) for DNMT3B (ab16049; Abcam, Cambridge, UK) and 4%–20% TGX Gel (Bio-Rad) for DNMT3A (2160S; Cell Signaling Technology, Danvers, MA, USA) and GAPDH (2118; Cell Signaling Technology).

Bisulfite sequencing

Bisulfite sequencing was conducted based on a method described in a previous report (Fukuda et al., 2021). Briefly, genomic DNA was extracted using the EZ DNA Methylation Kit (Zymo Research, Irvine, CA, USA). The amplified products were cloned into the pGEM-T Easy Vector System (Promega, Madison, WI, USA) by TA cloning or the PUC118 cloning vector (#3324; Takara Bio Inc., Siga, Japan) and sequenced. The results were analyzed using QUMA (http://quma.cdb.riken.jp/). The primer sequences are listed in Table S2.

Single-cell RNA-sequencing analysis

Sequencing using a 10× Chromium (10× Genomics, Pleasanton, CA, USA) platform was performed in Genewiz (Genewiz, South Plainfield, NJ, USA) based on the manufacturer's instructions. The Cell Ranger 3.1.0 pipeline (10× Genomics) was used for the alignment of the RNA sequence with the GRCh38 human reference genome. The default parameters were used to generate filtered gene expression matrix datasets. The datasets were loaded into R (https://www.r-project.org/), and the Seurat package (version 3 or 4) was used for transcriptomic analysis (Hao et al., 2021; Stuart et al., 2019). Cells with unique feature counts greater than 200 and less than 25% of mitochondrial counts were filtered, and the genes expressed in at least ten cells were used for UMAP analysis in hPSCs. Based on Seurat's default normalization methods, data from each hPSC line were merged using Seurat's merge function to plot cells from all hPSC lines. The clustering analysis for UMAP was performed using 20 dims with Seurat's RunUMAP function.

To calculate the X-linked gene dosage in hPSCs, the cells were filtered as described above. To exclude the cells showing potential initiation of differentiation, we removed the cells with less than 2 UMI (*OCT4* expression), so that more than 93% of cells were used for the X-linked gene expression analysis (Figure S1B). In *XIST* expression, as 0.01 was the threshold for *XIST* detection, we used it as the cut-off value for *XIST* expression (*XIST*+ cells: $\geq$ 0.01 and *XIST*– cells: < 0.01). A gene expression matrix with gene names was extracted using Seurat's GetAssayData function. The gene names were extracted from the matrix and annotated using the UCSC genome browser (https://genome.ucsc.edu/) to identify X-linked genes for the calculation. The extraction of expression data for X-linked genes and static analysis was performed using the default function of R. The raw and processed data were deposited in GEO (GSE186128).

In the public dataset analysis, the cortical organoid dataset from the HUES66 line was downloaded from Single Cell Portal (portals.broadinstitute.org/single_cell/study/reproducible-brain-organoids). The data were loaded in R and re-analyzed using Seurat. In the trajectory analysis, we used Monocle3(Cao et al., 2019) and calculated the pseudotime scores.

For *in vivo* data analysis, we used the human cell landscape dataset (GSE134355) and ileal uninvolved tissue samples (GSE134809). In the GSE134355 datasets, we obtained only female samples. The gene expression matrix was loaded into R, converted to a Seurat object, and normalized using Seurat's default function. The cells were screened based on the above parameters, considering cells without OCT4 expression and mitochondrial gene selection, because OCT4 is a pluripotent cell marker and *ACE2* expression affects mitochondrial activity (Shi et al., 2018). In cell type classifications, we used Seurat's FindMarkers function with MAST to identify marker genes (Table S1). Based on findings from previous reports (Bhaduri et al., 2020; Thomsen et al., 2016; Velasco et al., 2019), the cells were separated into each cell type.

For the calculation of the median expression levels of each X-linked gene excluding the *XIST* gene, the cells in each cluster were divided into either the *XIST*+ or – group using Seurat's subset function, and then the gene expression matrix was extracted using Seurat's Getassaydata function. Using the extracted gene expression matrix in R, the median expression levels of X-linked genes in at least more than 20 cells (for HUES66 data) or more than ten cells (*in vivo* data) in both *XIST*+ and – groups were calculated. For the analysis of the cell-type status based on *XIST* expression, the percentages of *XIST*+ or – cells in each cluster were calculated, and the $\log_2$ ratios were shown in figures. The median expression data are shown as heatmaps in figures using R.

The gene expression data in all scRNA-seq analysis in the present study is deposited at Mendeley and the DOI is listed in the key resources table. The related statistical data is provided in Table S3.

Module score calculation

Each module score in female hPSCs was calculated using the AddModuleScore function in Seurat with default parameters. The genes used for the differentiation modules were reported previously (Bock et al., 2011), and OCT4, SOX2, and NANOG were used for the core pluripotency module.

Bulk RNA-sequencing

RNA-sequencing analysis using bulk samples has been reported previously (Fukuda et al., 2021). Briefly, total RNA from the hPSC line (SEES5 background: wild-type, DNMT3A/3B DKO mutants) was extracted using the RNeasy Plus Micro Kit (Qiagen, Hilden, Germany), and polyA mRNA selection was used to generate the sequence library. The sequencing and read count data alignment with the human reference genome (hg38) were performed in Genewiz (Genewiz). The read count data were normalized by the trimmed mean of M-values normalization using the edgeR package (McCarthy et al., 2012). Hierarchical clustering analysis was performed using R's hclust function. The raw and processed data were deposited in GEO (GSE186128).

Quantification and statistical analysis

We used Seurat package in all statistical analyses in scRNA-seq data. For pair-wise comparison between *XIST*+ and - cells and multiple comparisons among the samples, we used Wilcoxon rank sum test and ANOVA with post-hoc test, respectively. In HUES66 and *in vivo* samples, FindMarkers function (MAST package) implemented in Seurat was used to identify the differentially expressed genes. All statistical data in the scRNA-seq analysis was shown in Table S3. For the data of neuronal differentiation assays, cell number analysis, and erosion induction tests, we performed paired, two-tailed t-tests to calculate p-values using R. p-values less than 0.05 were considered significant. The number of analyzed cells or genes was shown in figure legends.

Cell Reports Methods, Volume *2*

Supplemental information

De-erosion of X chromosome dosage compensation by the editing of *XIST* regulatory regions restores the differentiation potential in hPSCs

Nami Motosugi, Akiko Sugiyama, Chisa Okada, Asako Otomo, Akihiro Umezawa, Hidenori Akutsu, Shinji Hadano, and Atsushi Fukuda

Figure S1

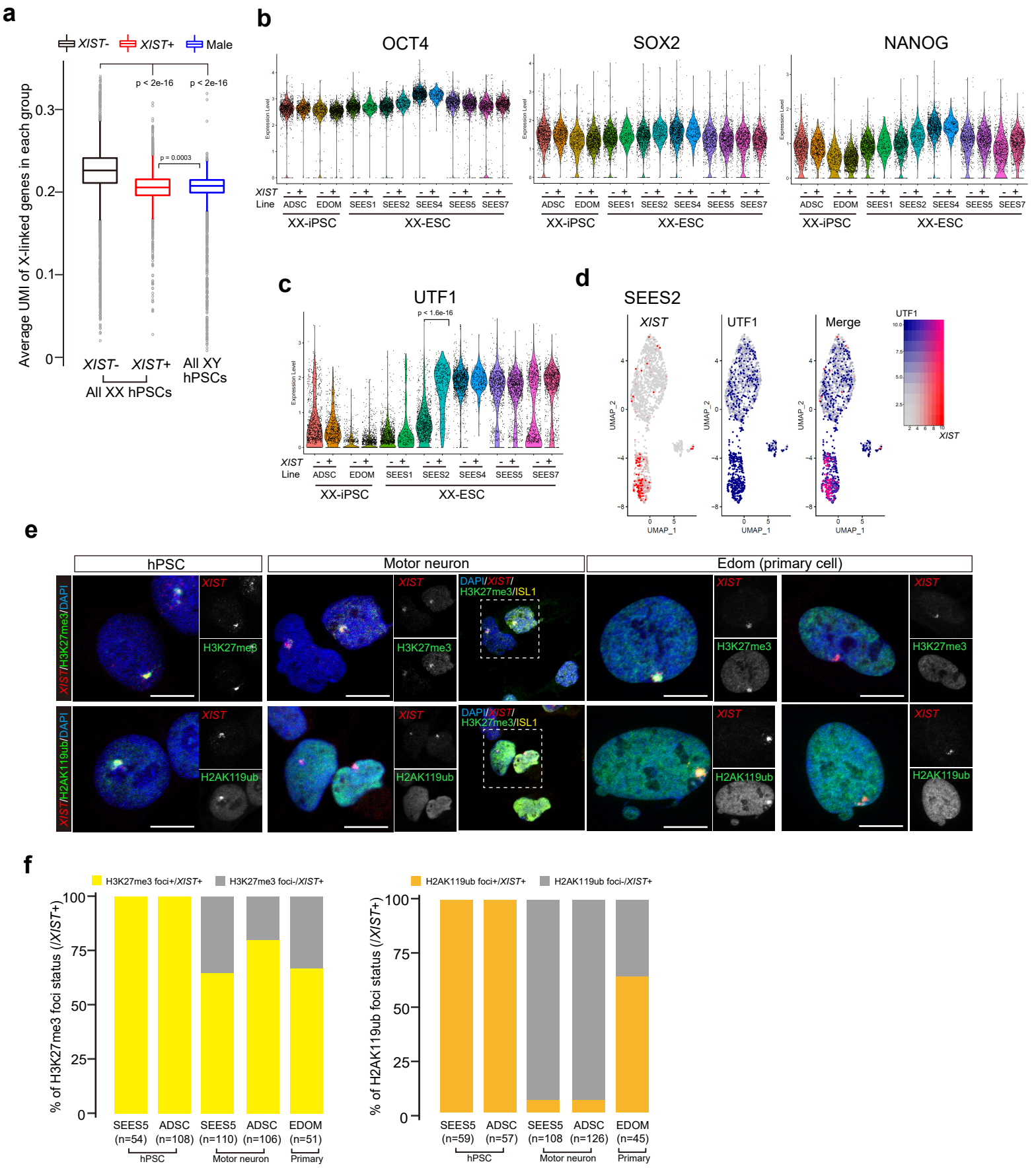
a
XIST-
XIST+
Male
p < 2e-16
p < 2e-16
p = 0.0003
Average UMI of X-linked genes in each group
0
0.1
0.2
0.3
XIST-
XIST+
All XY hPSCs
All XX hPSCs
b
OCT4
SOX2
NANOG
Expression Level
XIST
Line
ADSC
EDOM
SEES1
SEES2
SEES4
SEES5
SEES7
XX-iPSC
XX-ESC
c
UTF1
p < 1.6e-16
d
SEES2
XIST
UTF1
Merge
UMAP_1
UMAP_2
e
hPSC
Motor neuron
Edom (primary cell)
XIST/H3K27me3/DAPI
XIST/H2AK119ub/DAPI
DAPI/XIST/H3K27me3/ISL1
f
H3K27me3 foci+/XIST+
H3K27me3 foci-/XIST+
% of H3K27me3 foci status (/XIST+)
SEES5 (n=54)
ADSC (n=108)
SEES5 (n=110)
ADSC (n=106)
EDOM (n=51)
hPSC
Motor neuron
Primary
H2AK119ub foci+/XIST+
H2AK119ub foci-/XIST+
% of H2AK119ub foci status (/XIST+)
SEES5 (n=59)
ADSC (n=57)
SEES5 (n=108
ADSC (n=126)
EDOM (n=45)

Figure S1 related to Figure 1. Expression status of core pluripotency factors in *XIST*+ and – female hPSCs and changes in epigenetic modifications on Xi in each cell type. (**a**) Average X-linked gene expression status in male and female hPSCs. In females, the individual cells were separated into two groups based on the *XIST* expression status (*XIST*+ or –). *p*-values were calculated using one way ANOVA with post-hoc test. (**b**) Expression status of core pluripotency factors. The expression statuses of OCT4, SOX2, NANOG based on *XIST* expression in each line are shown. (**c**) UTF1 expression status. *p*-values were calculated using the Wilcoxon's rank-sum test. (**d**) UTF1 and *XIST* expression status in SEES2 line. The expression levels of each gene corresponded with the heatmap. (**e** and **f**) Immuno-FISH analysis for H3K27me3, H2AK119ub, and *XIST* in hPSCs, motor neurons, and menstrual blood-derived cells (primary EDOM). Motor neurons were identified by co-staining with ISL1. Representative images (e) and quantifications results (f) are shown. n refers to the number of cells analyzed.

Figure S2

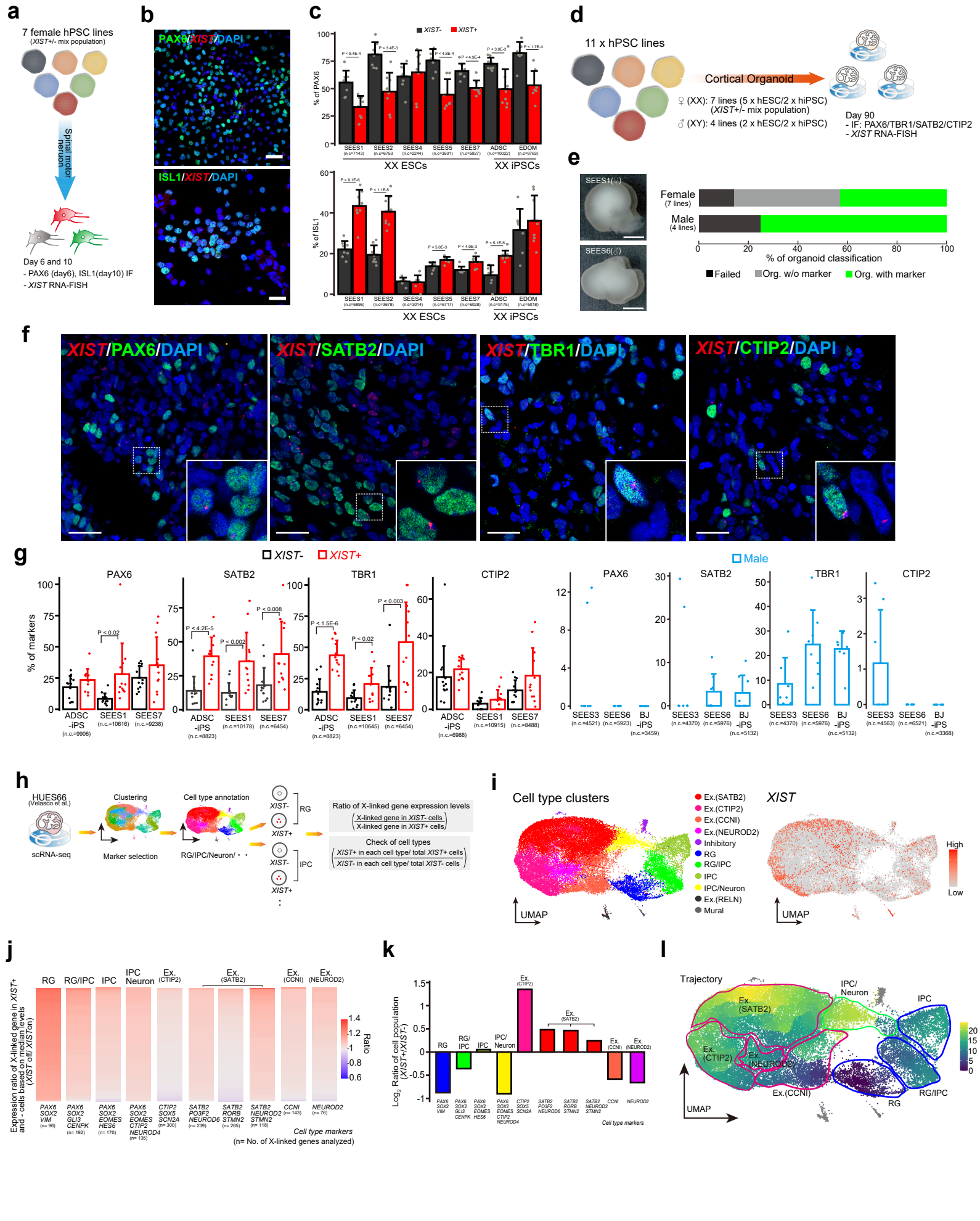
a
7 female hPSC lines
(XIST+/- mix population)
Spinal motor neuron
Day 6 and 10
- PAX6 (day6), ISL1(day10) IF
- XIST RNA-FISH
b
PAX6/XIST/DAPI
ISL1/XIST/DAPI
c
XIST-
XIST+
% of PAX6
% of ISL1
SEES1 (n.c=7143)
SEES2 (n.c=8753)
SEES4 (n.c=2244)
SEES5 (n.c=3501)
SEES7 (n.c=6827)
ADSC (n.c=10022)
EDOM (n.c=9763)
SEES1 (n.c=6896)
SEES2 (n.c=3678)
SEES4 (n.c=3014)
SEES5 (n.c=6717)
SEES7 (n.c=6028)
ADSC (n.c=9175)
EDOM (n.c=5018)
XX ESCs
XX iPSCs
d
11 x hPSC lines
Cortical Organoid
♀ (XX): 7 lines (5 x hESC/2 x hiPSC)
(XIST+/- mix population)
♂ (XY): 4 lines (2 x hESC/2 x hiPSC)
Day 90
- IF: PAX6/TBR1/SATB2/CTIP2
- XIST RNA-FISH
e
SEES1(♀)
SEES6(♂)
Female
(7 lines)
Male
(4 lines)
% of organoid classification
Failed
Org. w/o marker
Org. with marker
f
XIST/PAX6/DAPI
XIST/SATB2/DAPI
XIST/TBR1/DAPI
XIST/CTIP2/DAPI
g
XIST-
XIST+
Male
PAX6
SATB2
TBR1
CTIP2
% of markers
ADSC -iPS (n.c=9906)
SEES1 (n.c=10616)
SEES7 (n.c=9238)
ADSC -iPS (n.c=8823)
SEES1 (n.c=10178)
SEES7 (n.c=6454)
ADSC -iPS (n.c=8823)
SEES1 (n.c=10645)
SEES7 (n.c=6454)
ADSC -iPS (n.c=6988)
SEES1 (n.c=10915)
SEES7 (n.c=8488)
SEES3 (n.c=4521)
SEES6 (n.c=5923)
BJ -iPS (n.c=3459)
SEES3 (n.c=4370)
SEES6 (n.c=5976)
BJ -iPS (n.c=5132)
SEES3 (n.c=4370)
SEES6 (n.c=5976)
BJ -iPS (n.c=5132)
SEES3 (n.c=4563)
SEES6 (n.c=6521)
BJ -iPS (n.c=3368)
h
HUES66
(Velasco et al.)
scRNA-seq
Clustering
Marker selection
Cell type annotation
RG/IPC/Neuron/ · ·
XIST-
XIST+
RG
IPC
Ratio of X-linked gene expression levels
(X-linked gene in XIST- cells / X-linked gene in XIST+ cells)
Check of cell types
(XIST+ in each cell type/ total XIST+ cells / XIST- in each cell type/ total XIST- cells)
i
Cell type clusters
Ex.(SATB2)
Ex.(CTIP2)
Ex.(CCNI)
Ex.(NEUROD2)
Inhibitory
RG
RG/IPC
IPC
IPC/Neuron
Ex.(RELN)
Mural
XIST
High
Low
UMAP
UMAP
j
RG
RG/IPC
IPC
IPC Neuron
Ex. (CTIP2)
Ex. (SATB2)
Ex. (CCNI)
Ex. (NEUROD2)
Expression ratio of X-linked gene in XIST+ and - cells based on median levels (XIST off/ XIST on)
Ratio
PAX6 SOX2 VIM (n= 96)
PAX6 SOX2 GLI3 CENPK (n= 192)
PAX6 SOX2 EOMES HES6 (n= 170)
PAX6 SOX2 EOMES CTIP2 NEUROD4 (n= 135)
CTIP2 SOX5 SCN2A (n= 300)
SATB2 POU3F2 NEUROD6 (n= 239)
SATB2 RORB STMN2 (n= 265)
SATB2 NEUROD2 STMN2 (n= 118)
CCNI (n= 143)
NEUROD2 (n= 76)
Cell type markers
(n= No. of X-linked genes analyzed)
k
Log2 Ratio of cell population (XIST+/XIST-)
RG
RG/ IPC
IPC
IPC/ Neuron
Ex. (CTIP2)
Ex. (SATB2)
Ex. (CCNI)
Ex. (NEUROD2)
PAX6 SOX2 VIM
PAX6 SOX2 GLI3 CENPK
PAX6 SOX2 EOMES HES6
PAX6 SOX2 EOMES CTIP2 NEUROD4
CTIP2 SOX5 SCN2A
SATB2 POU3F2 NEUROD6
SATB2 RORB STMN2
SATB2 NEUROD2 STMN2
CCNI
NEUROD2
Cell type markers
l
Trajectory
IPC/ Neuron
IPC
Ex. (SATB2)
Ex. (CTIP2)
Ex. (NEUROD2)
Ex.(CCNI)
RG/IPC
RG
UMAP
Pseudotime

Figure S2 related to Figure 2. *XIST* expression status is linked to the stages of neuronal differentiation. (**a**) Experimental scheme for MN differentiation from hPSCs using a 2D culture protocol. (**b** and **c**) Immunofluorescence combined with *XIST* RNA-FISH analysis in differentiating cells. The picture shows the representative image (b), and the quantification results are shown as bar graphs (c). The percentage of PAX6+ or ISL1+ cells among *XIST*+ or – cells was calculated. Each dot and n.c indicate the percentage in the observed area and the total number of cells analyzed, respectively. p-values are calculated using Student's *t*-test. Scale bar represents 50 μm. (**d**) Experimental scheme for generating cortical organoids from hPSCs. On day 90, the samples were subjected to immuno-*XIST* RNA-FISH analysis. Representatives for progenitor cell (PAX6) and cortical layers (SATB2, CTIP2, and TBR1) were used. (**b**) Representative image of a cortical organoid and developmental summary at day 90. Scale bar represents 1 mm. (**c**) Representative images of immuno-*XIST* RNA-FISH analysis in cortical organoid samples. Scale bar represents 50 μm. (**d**) Quantification results of each marker. In female samples, the marker expression status was based on *XIST* expression. Each dot and n.c indicate the percentage in the observed area and the total number of cells analyzed, respectively. Error bars show the standard deviation. *p*-values are calculated by Student's *t*-test. (**h**) Experimental scheme for analyzing cell types based on the *XIST* expression status in the HUES66 line (Velasco *et al.*, 2019). For analysis of the ratio of X-linked gene expression levels, X-linked genes expressed in at least 20 cells in both *XIST*+ and – groups were used. The ratios were based on the median expression levels. Each cell type annotation was based on a previous report (Bhaduri *et al.*, 2020), and the marker genes used for classifications were identified using MAST. (**i**) UMAP based on cell types (left) and *XIST* expression (right). RG; radial glia, IPC; intermediate progenitor cell, Ex.; excitatory. Ex. Inhibitory; inhibitory neuron. (**j**) Expression ratio of X-linked genes in *XIST*+ and – cells based on median levels. The heatmap shows the ratio of X-linked genes (*XIST*-/*XIST*+), indicating that red is overexpressed in *XIST*- cells. n refers to the number of X-linked genes analyzed. Representative marker genes used for the classifications are shown as cell type markers. SATB2 cells were separated into three types based on the markers. (**k**) The ratio of cell types based on the *XIST* expression status. Log_2 ratio (*XIST*+/*XIST*-) was shown in each cell type. (**l**) Trajectory analysis of cortical organoid. Pseudotime was calculated and the cells were highlighted based on the scores.

Figure S3

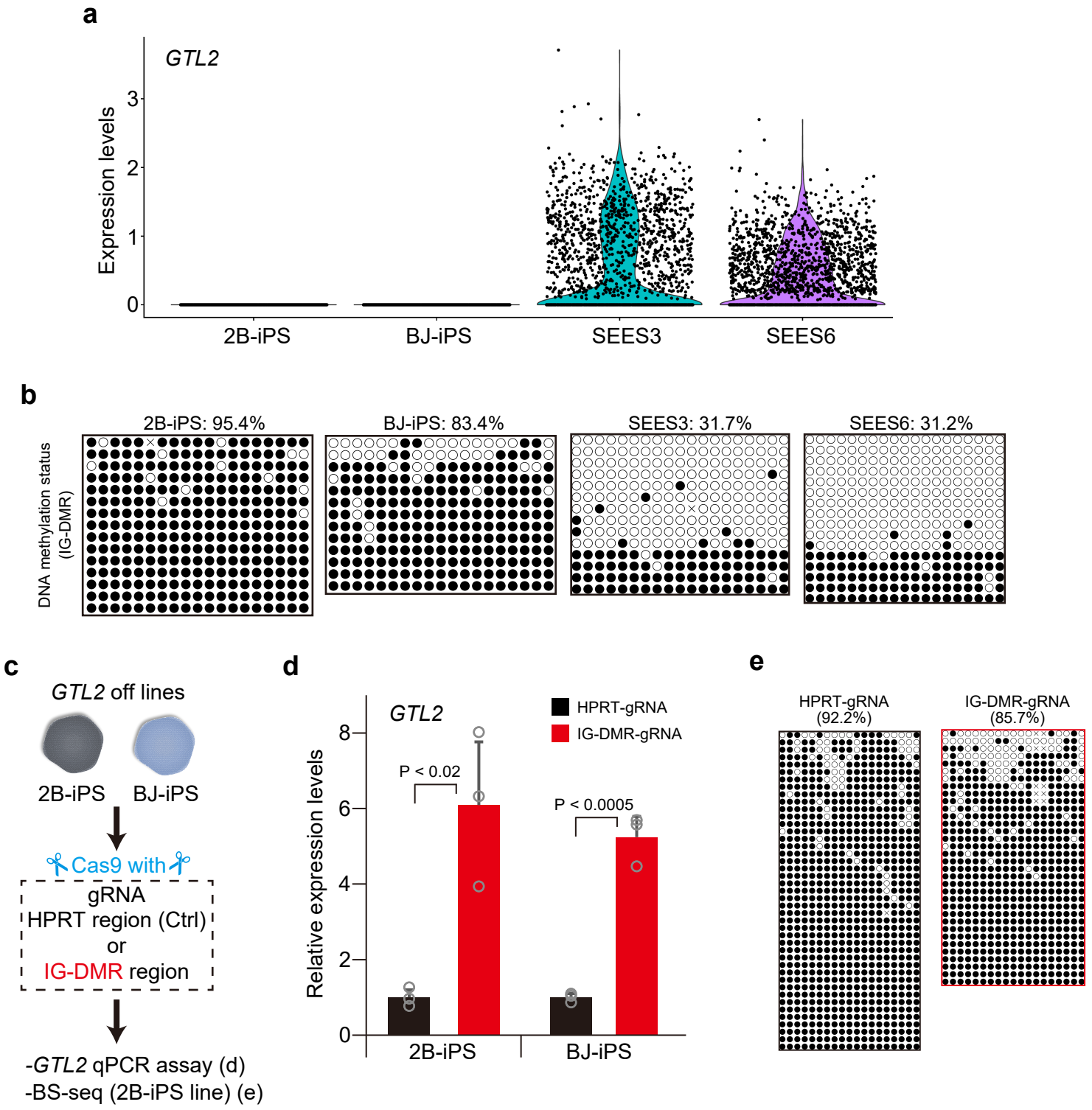
a
GTL2
Expression levels
0
1
2
3
2B-iPS
BJ-iPS
SEES3
SEES6
b
DNA methylation status (IG-DMR)
2B-iPS: 95.4%
BJ-iPS: 83.4%
SEES3: 31.7%
SEES6: 31.2%
c
GTL2 off lines
2B-iPS
BJ-iPS
Cas9 with
gRNA
HPRT region (Ctrl)
or
IG-DMR region
-GTL2 qPCR assay (d)
-BS-seq (2B-iPS line) (e)
d
GTL2
HPRT-gRNA
IG-DMR-gRNA
Relative expression levels
P < 0.02
P < 0.0005
0
2
4
6
8
2B-iPS
BJ-iPS
e
HPRT-gRNA (92.2%)
IG-DMR-gRNA (85.7%)

Figure S3 related to Figure 3. Reactivation of methylated *GTL2* by Cas9-mediated DSB. (**a**) *GTL2* expression in male hiPSC lines. Single-cell RNA-sequencing (scRNA-seq) data are shown. *GTL2* was not detected in hiPSC lines. (**b**) BS analysis of IG-DMR in *GTL2*^{off} and *GTL2*^{on} lines. (**c**) Experimental scheme for *GTL2* reactivation and DNA demethylation by Cas9-mediated DSB. *GTL2*^{off} lines were used for the TaqMan gene expression assays (d) and BS-seq analysis (e). gRNA targeting *HPRT1* was used as a negative control. At 144 h after transfection, the cells were analyzed. (**d**) qPCR results for *GTL2* expression. The average expression level of the HPRT1-gRNA sample was set to 1 in each line. Each dot indicates an independent experiment. Error bars show the standard deviations. *p*-values were calculated using Student's *t*-test. (e) BS-seq analysis of IG-DMR in Cas9/gRNA transfected 2B-iPSCs.

Figure S4

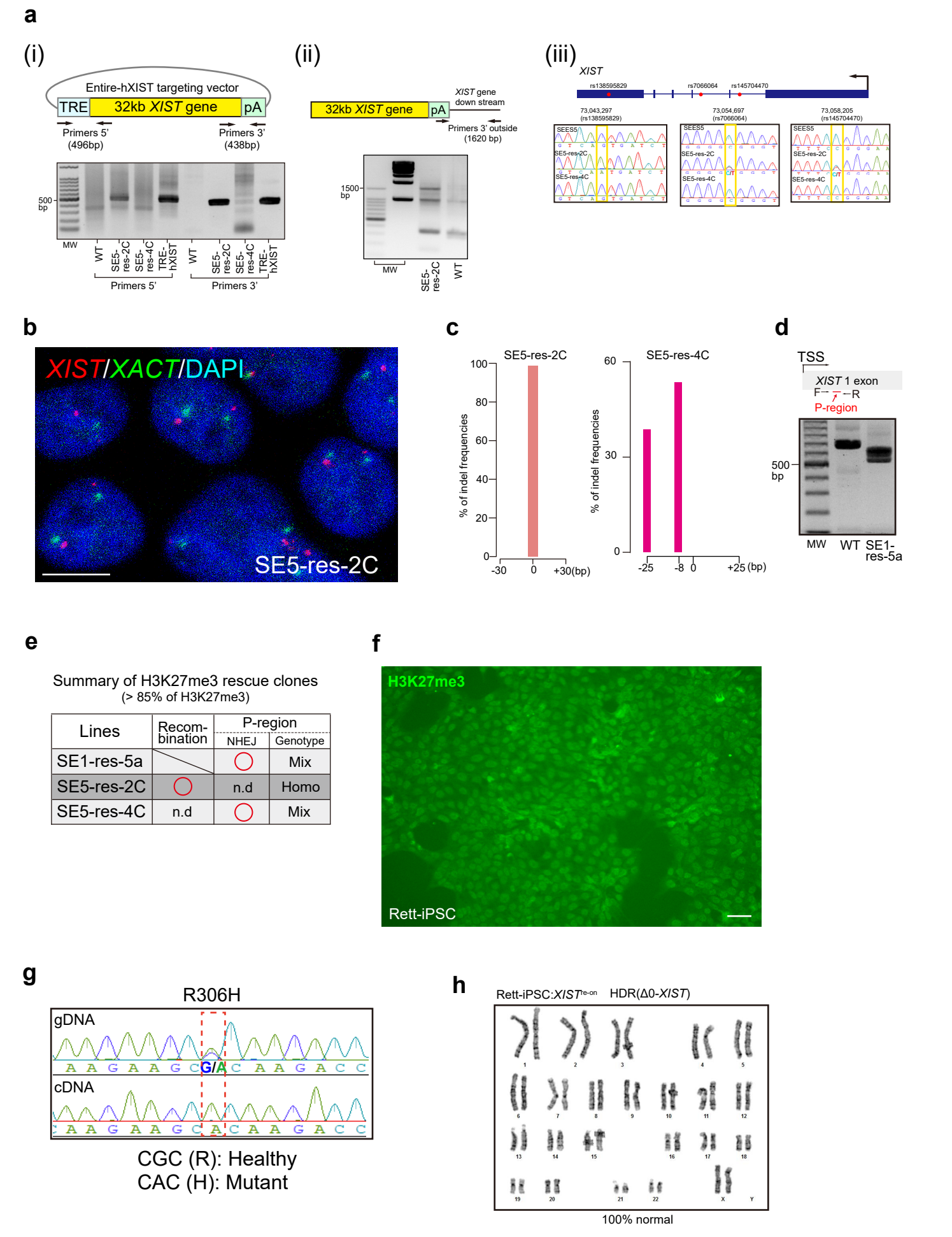
a
(i)
Entire-hXIST targeting vector
TRE
32kb XIST gene
pA
Primers 5'
(496bp)
Primers 3'
(438bp)
500 bp
MW
WT
SE5-res-2C
SE5-res-4C
TRE-hXIST
Primers 5'
Primers 3'
(ii)
32kb XIST gene
pA
XIST gene down stream
Primers 3' outside
(1620 bp)
1500 bp
MW
SE5-res-2C
WT
(iii)
XIST
rs138595829
rs7066064
rs145704470
73,043,297 (rs138595829)
73,054,697 (rs7066064)
73,058,205 (rs145704470)
SEES5
SE5-res-2C
SE5-res-4C
b
XIST/XACT/DAPI
SE5-res-2C
c
SE5-res-2C
% of indel frequencies
100
80
60
40
20
0
-30
0
+30(bp)
SE5-res-4C
% of indel frequencies
60
30
0
-25
-8
0
+25 (bp)
d
TSS
XIST 1 exon
F
R
P-region
500 bp
MW
WT
SE1-res-5a
e
Summary of H3K27me3 rescue clones
(> 85% of H3K27me3)
Lines
Recom-bination
P-region
NHEJ
Genotype
SE1-res-5a
Mix
SE5-res-2C
n.d
Homo
SE5-res-4C
n.d
Mix
f
H3K27me3
Rett-iPSC
g
R306H
gDNA
A A G A A G C G/A C A A G A C C
cDNA
A A G A A G C A C A A G A C C
CGC (R): Healthy
CAC (H): Mutant
h
Rett-iPSC:XIST re-on
HDR(Δ0-XIST)
100% normal

Figure S4 related to Figure 3 and 4. Genotyping and DNAme status in *XIST* re-expressed lines and characterization of Rett-iPSCs. (**a**) Genotyping PCR analysis of *XIST* re-expressing lines in SEES5 cells. TRE and SV40 sequences were included in Entire-hXIST vector (i and ii). Sanger sequencing analysis of SNVs (iii). (**b**) DNA-FISH assay using *XIST* and *XACT* probes in SE5-res-2C. The scale bar represents 10 μm. (**c**)TIDE analysis for checking scars. The mutant allele was not detected in the SE5-res-2C line, whereas the SE5-res-4C line comprised cells with two different alleles. (**d**) Genotyping PCR spanning the P-region in SE1-res-5a. (**e**)Summary of the obtained H3K27me3 foci rescue clones. Mix refers to two different alleles identified by TIDE analysis or Sanger sequences. n.d. refers to not determined. (**f**) H3K27me3 staining of Rett-iPSC. Scale bar represents 50 μm. (**g**) Genotyping and expression allele analysis using gDNA and cDNA. The mutation point is highlighted in the red dashed line. (**h**) G-band analysis of the Rett-iPSC: *XIST*$^{re\text{-}on}$ (Δ0-*XIST*).

Figure 5

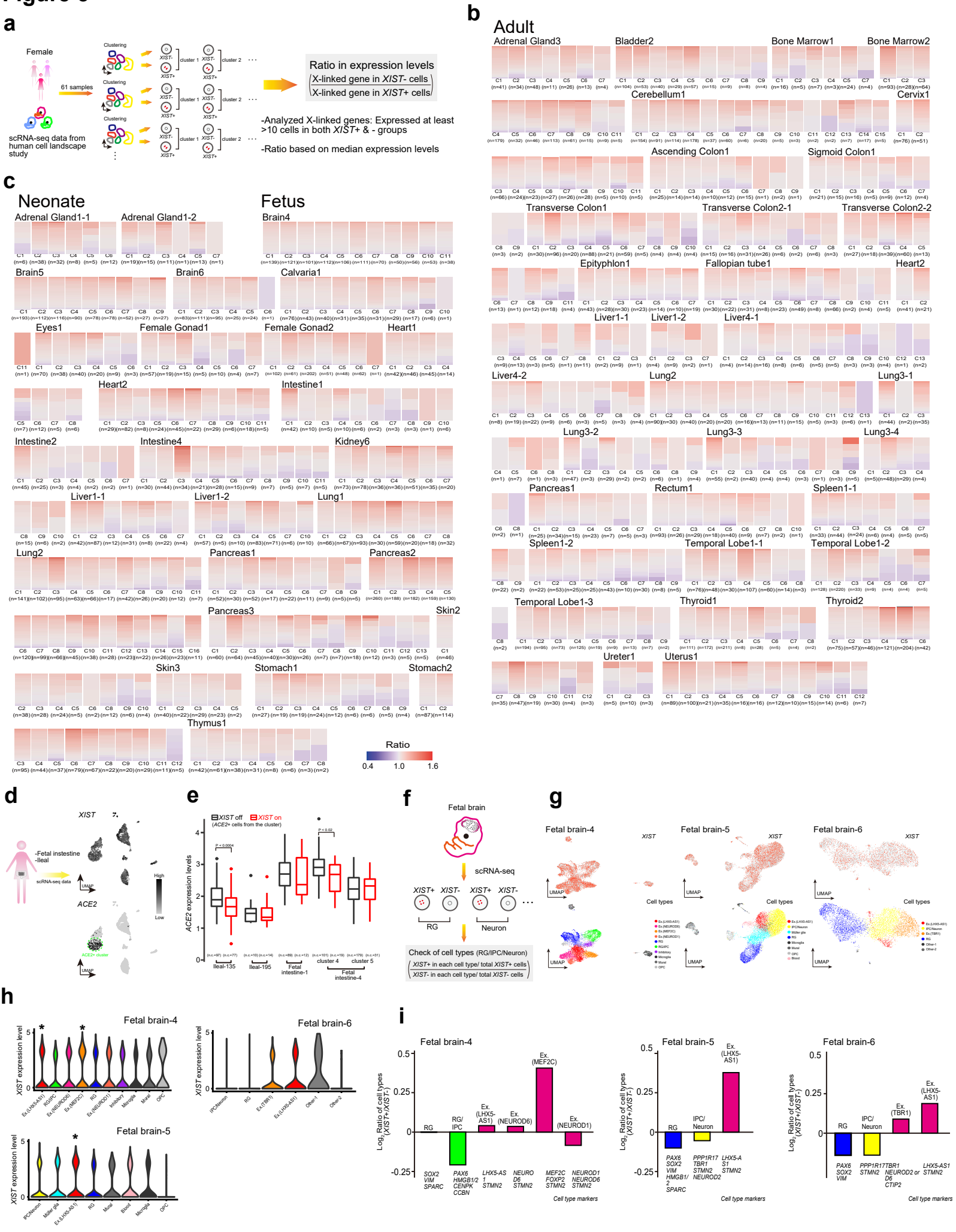
a
Female
61 samples
scRNA-seq data from human cell landscape study
Clustering
cluster 1
cluster 2
Ratio in expression levels
(X-linked gene in XIST- cells / X-linked gene in XIST+ cells)
-Analyzed X-linked genes: Expressed at least >10 cells in both XIST+ & - groups
-Ratio based on median expression levels
b
Adult
Adrenal Gland3
Bladder2
Bone Marrow1
Bone Marrow2
Cerebellum1
Cervix1
Ascending Colon1
Sigmoid Colon1
Transverse Colon1
Transverse Colon2-1
Transverse Colon2-2
Epityphlon1
Fallopian tube1
Heart2
Liver1-1
Liver1-2
Liver4-1
Liver4-2
Lung2
Lung3-1
Lung3-2
Lung3-3
Lung3-4
Pancreas1
Rectum1
Spleen1-1
Spleen1-2
Temporal Lobe1-1
Temporal Lobe1-2
Temporal Lobe1-3
Thyroid1
Thyroid2
Ureter1
Uterus1
c
Neonate
Adrenal Gland1-1
Adrenal Gland1-2
Brain5
Brain6
Calvaria1
Eyes1
Female Gonad1
Female Gonad2
Heart1
Heart2
Intestine1
Intestine2
Intestine4
Kidney6
Liver1-1
Liver1-2
Lung1
Lung2
Pancreas1
Pancreas2
Pancreas3
Skin2
Skin3
Stomach1
Stomach2
Thymus1
Fetus
Brain4
Ratio
0.4
1.0
1.6
d
XIST
-Fetal instestine
-Ileal
scRNA-seq data
UMAP
ACE2
High
Low
ACE2+ cluster
e
XIST off
XIST on
(ACE2+ cells from the cluster)
ACE2 expression levels
P < 0.0004
P < 0.02
Ileal-135
Ileal-195
Fetal intestine-1
cluster 4
cluster 5
Fetal intestine-4
f
Fetal brain
scRNA-seq
XIST+
XIST-
RG
Neuron
Check of cell types (RG/IPC/Neuron)
(XIST+ in each cell type/ total XIST+ cells)
(XIST- in each cell type/ total XIST- cells)
g
Fetal brain-4
Fetal brain-5
Fetal brain-6
UMAP
Cell types
h
Fetal brain-4
Fetal brain-6
Fetal brain-5
XIST expression level
i
Fetal brain-4
Fetal brain-5
Fetal brain-6
Log2(Ratio of cell types (XIST+/XIST-))
RG
RG/ IPC
Ex. (LHX5-AS1)
Ex. (NEUROD6)
Ex. (MEF2C)
Ex. (NEUROD1)
IPC/ Neuron
Ex. (TBR1)
SOX2 VIM SPARC
PAX6 HMGB1/2 CENPK CCBN
LHX5-AS1 STMN2
NEUROD6 STMN2
MEF2C FOXP2 STMN2
NEUROD1 NEUROD6 STMN2
PAX6 SOX2 VIM HMGB1/2 SPARC
PPP1R17 TBR1 STMN2 NEUROD2
LHX5-AS1 STMN2
PAX6 SOX2 VIM
PPP1R17 STMN2
TBR1 NEUROD2 or D6 CTIP2
LHX5-AS1 STMN2
Cell type markers

Figure S5 related to Figure 1, 2 and 5. Effect of the *XIST* expression status *in vivo*. (**a**) Analysis scheme using 61 scRNA-seq datasets from human cell atlas (Han *et al.*, 2020). (**b** and **c**) The ratios (*XIST*– cells/*XIST*+ cells) in adult tissues (b) and neonatal and fetal tissues (c). C and n indicate the cluster identity and number of X-linked genes analyzed, respectively. (**d**) Experimental scheme for identifying *ACE2*+ clusters from the fetal intestine and ileal cells. The representative images of UMAP analysis with *XIST* and *ACE2* expression are shown. The *ACE2*+ clusters were identified by MAST analysis. (**e**) *ACE2* expression status based on the *XIST* expression levels. The cells from *ACE2*+ clusters were isolated, and the *ACE2* expression levels were compared based on the *XIST* expression status. n.c. refers to the number of cells analyzed. *p*-values were calculated using the Wilcoxon's rank-sum test. (**f**) Experimental scheme for evaluating neuronal development in vivo based on the *XIST* expression status. Three fetal brain samples were used. The gene sets for cell-type annotation were identified by MAST analysis and classifications were based on the previously identified markers (Bhaduri *et al.*, 2020; Camp et al., 2015). (**g**) UMAP analysis. The *XIST* expression status (upper) and cell types were highlighted by each color (bottom). (**h**) The *XIST* expression levels in each cell type based on scRNA-seq results. The violin plot shows the *XIST* expression status in each cell type. Asterisks indicate statistical significance determined using MAST test with Bonferroni correction. All p-values were < 7.4 E-9. (**i**) The ratio of cell types based on the *XIST* expression status. Log_2 ratio (*XIST*+/*XIST*-) was shown in each cell type. The representative marker genes used for the classification were shown.